Cell Reports
Medicine

Article

Selective apoptosis of tumor-associated platelets boosts the anti-metastatic potency of PD-1 blockade therapy

Graphical abstract

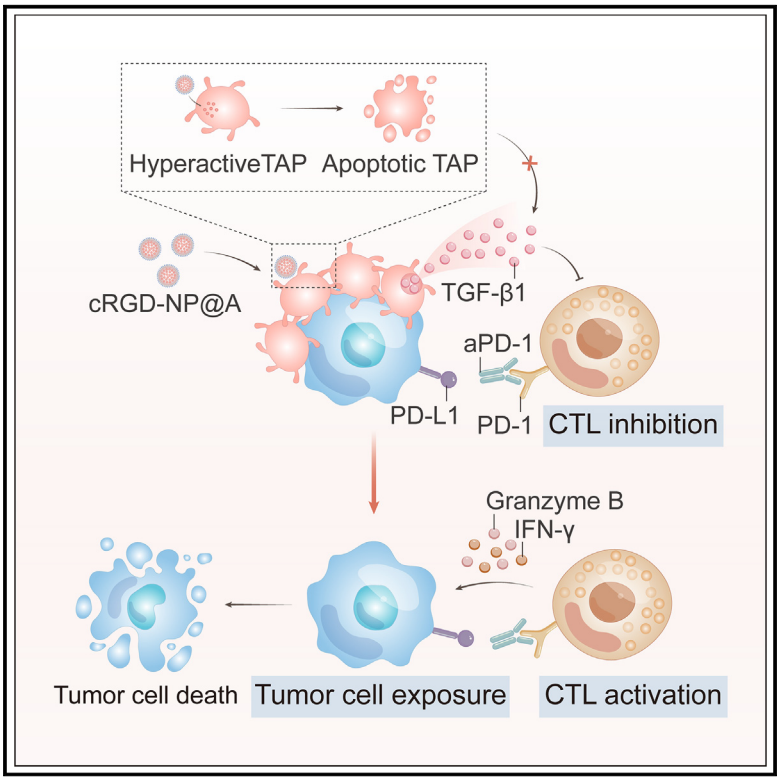

Highlights

- cRGD-NP@A selectively induces apoptosis in hyperactive TAPs
- cRGD-NP@A disrupts platelet-tumor cell interactions, inhibiting tumor metastasis
- cRGD-NP@A improves the anti-metastatic efficacy of PD-1 blockade therapy
- cRGD-NP@A boosts immune surveillance and reduces TGF-β1 secretion

Authors

Suying Wu, Zhouliang Wu, Zefang Lu, ..., Yuliang Zhao, Guangjun Nie, Suping Li

Correspondence

lisuping@nanoctr.cn

In brief

Wu et al. develop cRGD-NP@A, a polymeric nanomedicine that selectively induces apoptosis in hyperactive tumor-associated platelets (TAPs). By disrupting platelet-tumor interactions and reducing TAP-derived immunosuppressive factors, cRGD-NP@A enhances PD-1 blockade therapy, improving its anti-metastatic efficacy in preclinical models.

Wu et al., 2025, Cell Reports Medicine 6, 101984
March 18, 2025
https://doi.org/10.1016/j.xcrm.2025.101984

CellPress

Cell Reports Medicine

CellPress
OPEN ACCESS

Article

Selective apoptosis of tumor-associated platelets boosts the anti-metastatic potency of PD-1 blockade therapy

Suying Wu,[1,2,6] Zhouliang Wu,[3,6] Zefang Lu,[1,2] Feilong Qi,[1] Jin Cheng,[1,2] Tianjiao Chu,[1,4] Bozhao Li,[1] Yuliang Zhao,[1,2,5] Guangjun Nie,[1,2] and Suping Li[1,2,7,*]

[1]CAS Key Laboratory for Biomedical Effects of Nanomaterials and Nanosafety, CAS Center for Excellence in Nanoscience, National Center for Nanoscience and Technology, Beijing 100190, P.R. China

[2]Center of Materials Science and Optoelectronics Engineering, University of Chinese Academy of Sciences, Beijing 100049, P.R. China

[3]Department of Urology, Tianjin Institute of Urology, The Second Hospital of Tianjin Medical University, Tianjin Medical University, Tianjin 300211, P.R. China

[4]School of Astronautics, Harbin Institute of Technology, Harbin 150001, P.R. China

[5]School of Chemistry and Chemical Engineering, Guangzhou University, Guangzhou 510006, P.R. China

[6]These authors contributed equally

[7]Lead contact

*Correspondence: lisuping@nanoctr.cn

https://doi.org/10.1016/j.xcrm.2025.101984

SUMMARY

Despite the transformative impact of programmed cell death protein-1 (PD-1) blockade therapy on metastatic/advanced solid tumor treatment, its efficacy is hindered by a limited response rate. Platelets play a pivotal role in tumor metastasis by shielding circulating tumor cells and secreting immunosuppressive factors. We here demonstrate that selectively inducing apoptosis in tumor-associated platelets (TAPs) using ABT-737-loaded nanoparticles (cyclic arginine-glycine-aspartate containing peptide-modified ABT-737-loaded nanoparticles [cRGD-NP@A]) enhances the anti-metastatic efficacy of the anti-PD-1 antibody (aPD-1). cRGD-NP@A specifically binds to TAPs, disrupting platelet-tumor cell interactions and exposing tumor cells to immune surveillance *in vivo*. Combined with aPD-1, cRGD-NP@A substantially augments immune activation and reduces TAP-derived immunosuppressive factors, notably transforming growth factor β1 (TGF-β1), consequently improving anti-metastatic outcomes across multiple metastasis-bearing animal models without observable adverse effects. Our study underscores the importance of depleting TAPs to enhance PD-1 blockade therapy, presenting a promising strategy to improve response rates and clinical outcomes for patients with metastatic cancer.

INTRODUCTION

Metastasis, a hallmark of cancer, stands as the leading cause of cancer-related deaths and remains a major challenge for cancer treatment.[1] The interaction between programmed cell death protein ligand-1 (PD-L1) on tumor cells and the immune checkpoint programmed cell death protein-1 (PD-1) on T cells aids tumor cells in evading immune destruction, facilitating successful metastasis.[2–4] PD-1/PD-L1 inhibitors, which can disrupt this interaction, have transformed the treatment landscape for metastatic/advanced solid tumors, with favorable safety profiles.[5] Yet, their response rate is limited, benefiting only a small proportion of patients with metastatic cancer. Elevating the response rate to PD-1/PD-L1 inhibitors remains challenging for prolonging the overall survival of patients with cancer.

The metastatic cascade, wherein tumor cells spread from the primary tumors to surrounding tissues or distant organs, involves invasion, intravasation, circulation, extravasation, and colonization.[6] Platelets, the second most abundant cells in the blood, play a critical role in various stages of cancer metastasis.[7–9] In response to tumor-derived stimuli, platelets were found to have enhanced activity with upregulated adhesion protein expression and elevated secretion of bioactive factors from granules.[9–11] These alterations, leading to "tumor-educated platelets" or "tumor-associated platelets" (TAPs), facilitate tumor growth and metastasis.[12,13] Once tumor cells enter the bloodstream, TAPs serve as "first responders" by rapidly adhering to their surface to form protective hetero-aggregates within minutes, with tumor cells at the core.[14,15] These hetero-aggregates not only physically shield tumor cells from shear forces and immune surveillance but also provide an abundant source of adhesion proteins for blood vessel arrest in distant organs.[16–20] Furthermore, TAPs enhance tumor cell colonization at distant sites by inducing endothelial openings and forming pre-metastatic niches through the secretion of nucleotides and abundant immunosuppressive factors, especially transforming

growth factor β1 (TGF-β1), respectively.[14,21,22] Existing clinical evidence indicates that aggregates of tumor cells and hyperactive/activated platelets are frequently found in circulation, along with TAPs in metastatic foci.[23,24] The hyperactivity of circulating platelets and their prevalence in metastases have been linked to poor prognosis in patients with metastatic cancer,[25,26] underscoring platelets as an important target in metastatic cancer management. Despite PD-1/PD-L1 blockade, the persistence of this physical shielding and immunosuppressive microenvironment poses a significant challenge, leading to therapeutic failure. In addition to their well-established roles in hemostasis and tumor metastasis, platelets have also been recognized as versatile immune cells, exhibiting pro-inflammatory functions in conditions such as immunothrombosis and anti-inflammatory effects in maintaining circulating monocyte quiescence.[27,28] This underscores the importance of maintaining a normal platelet count to preserve both vascular and immune balance.

Inspired by these findings, we hypothesized that selectively inducing apoptosis in TAPs might promote immune cell recognition of metastatic tumor cells, reduce TGF-β1-mediated immune suppression, and, consequently, improve the efficacy of anti-PD-1 (aPD-1) treatment. To test our hypothesis, we constructed a polymeric nanoparticle loaded with ABT-737, a common platelet apoptosis inducer that functions by inhibiting the activity of anti-apoptotic protein BCL-xL in platelets,[29] using self-assembled biocompatible poly(lactic-co-glycolic acid) (PLGA) nanoparticles. Encapsulation of hydrophobic ABT-737 inside improved its bioavailability and safety. Additionally, we modified the nanoparticle surface with cyclic arginine-glycine-aspartate (cRGD)-containing peptide for specific targeting of TAPs. This modification facilitates nanoparticle binding and internalization by TAPs, enabling the release of encapsulated ABT-737 inside, thereby inducing apoptotic responses within these platelets. Systemic administration of the resulting formulation, cRGD-modified ABT-737-loaded nanoparticles (cRGD-NP@A), effectively disrupted platelet-tumor cell interactions, reduced platelet activation and TGF-β1 secretion, and consequently inhibited tumor metastasis in both metastatic tumor-bearing mouse and rat models without detectable bleeding risks. Further combination of cRGD-NP@A with aPD-1 antibody significantly enhanced immune activation and anti-metastatic efficacy of aPD-1, without causing additional side effects. Our study reveals a significant connection between TAP targeting and aPD-1 treatment efficacy, presenting a safe and promising strategy to enhance the response rates and clinical outcomes in patients with metastatic cancer undergoing PD-1 blockade therapy.

RESULTS

Investigation of tumor cell impact on platelet activity and construction of TAP-targeting nanoparticles

To verify the effect of tumor cells on platelet activity, we first co-incubated CellMask Orange-labeled platelets isolated from healthy C57BL/6N mice with murine B16-F10 melanoma cells. The co-incubation resulted in platelet activation within 1 h, and the activation level positively correlated with the duration of incubation, as demonstrated by the increased CD62P expression, a common surface marker of platelet activation (Figure S1A). Further, the platelets collected from mice bearing B16-F10 pulmonary metastasis showed an 8.7-fold increase in CD62P expression and a 2.2-fold enhanced response to the agonist ADP compared to those from healthy controls (Figures S1B and S1C). By contrast, the platelets from mice only bearing subcutaneous primary melanoma tumors exhibited slightly increased reactivity to ADP stimulation in contrast to control ones. Moreover, the JON/A antibody, which specifically recognizes the active form of the glycoprotein IIb/IIIa (GPIIb/IIIa) receptor, a well-known platelet activation marker, exhibited increased binding to platelets from B16-F10 metastasis-bearing mice, both with and without ADP stimulation (Figure S1D). The increased release of thrombospondin 1 and soluble CD62P into circulation further confirms platelet activation and hyperreactivity induced by metastatic melanoma *in vivo* (Figure S1E). Additionally, nearly all platelets within the tumor tissues showed clear expression of activated GPIIb/IIIa, indicating that tumor-infiltrating platelets are activated under the influence of the tumor microenvironment (TME) (Figure S1F). These results suggest that tumor cells have the capacity to trigger platelet activation and hyperreactivity both *in vitro* and *in vivo*, consistent with the findings reported in earlier studies.[10,30,31] Additionally, our results also reveal that metastatic tumors possess a greater propensity to prompt circulating platelets into a hyperreactive state compared to non-metastatic primary tumors, possibly attributed to the increased likelihood of direct contact between metastatic tumor cells and platelets.

To develop nanoparticles that effectively target TAPs, we first conducted a screening to identify the optimal peptide for guiding the nanoparticles to TAPs. We compared the targeting abilities of the cyclic arginine-glycine-aspartate containing CNPRGDY(OEt)RC peptide (cRGD) and P-selectin (CD62P)-targeting DAEWVDVS peptide (PSN) on both agonist- and tumor cell-stimulated platelets. Notably, the cRGD and PSN peptides were known to selectively bind to active GPIIb/IIIa (also known as integrin αIIbβ3) and CD62P, respectively, on activated/hyperactive platelet surfaces.[32,33] To effectively simulate the hyperactive state of TAPs *in vitro*, we employed ADP, a major platelet agonist secreted by tumor cells,[34,35] to activate platelets. Flow cytometry analysis demonstrated specific binding of cRGD peptide to ADP-activated platelets, as evidenced by a comparable level of CD62P-positive with cRGD-fluorescein isothiocyanate (FITC)-positive platelets, while negligible binding to resting platelets was observed (Figures S2A and S2B). Furthermore, cRGD-FITC rapidly bound to platelets stimulated by B16-F10 cells, whereas minimal binding was observed in unstimulated platelets (Figure S2C). In contrast, the attachment of PSN peptide to both ADP- and B16-F10-stimulated platelets was significantly weaker than those observed with cRGD. Notably, the cRGE control peptide (CNPRGEY(OEt)RC), in which the functional aspartate (D) residue in the cRGD sequence is substituted with glutamate (E), showed minimal binding to both resting and activated platelets (Figure S3A). Moreover, cRGD exhibited minimal binding to B16-F10 tumor cells, which express several integrins such as β1 and α5[36,37], resulting in fewer than 1% of cells positive for cRGD signal, highlighting its high specificity for targeting activated platelets (Figure S3B). These results underscore the stronger targeting ability of the cRGD peptide toward TAPs than the PSN peptide; thus, the cRGD peptide was

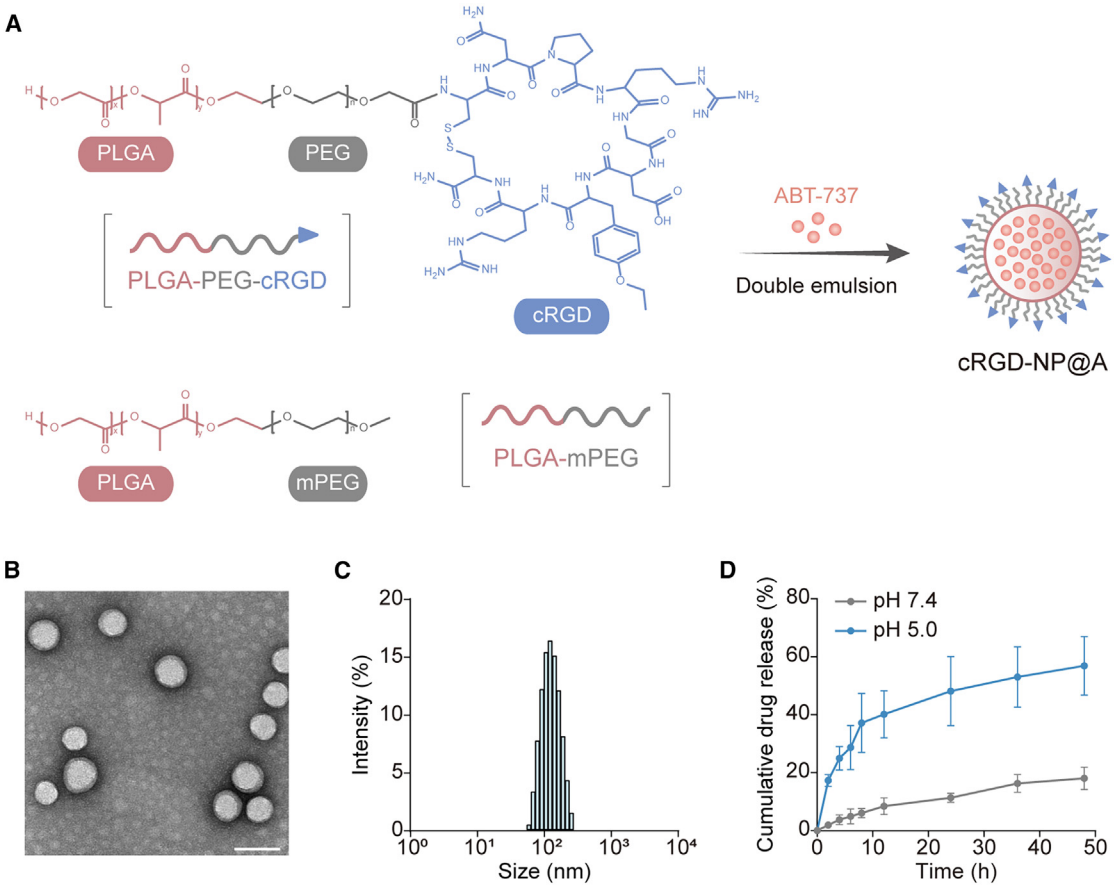

Figure 1. Preparation and characterization of the cRGD-NP@A nanoparticles

(A) Schematic illustration of the preparation of cRGD-NP@A.

(B) Representative TEM image of cRGD-NP@A. Scale bar, 100 nm.

(C) Size distribution of cRGD-NP@A analyzed using dynamic light scattering.

(D) *In vitro* drug release profile of ABT-737 from cRGD-NP@A at pH 7.4 and pH 5.0 within 48 h.

Data are presented as mean ± SD, $n = 3$ biological replicates.

See also Figures S1–S5.

employed for constructing TAP-targeting nanoparticles. The cRGD peptide was first conjugated with PLGA-PEG-NHS (PLGA-b-poly(ethylene glycol)-N-hydroxysuccinimide) to form PLGA-PEG-cRGD (Figures S4A and S4B). Flow cytometry analysis demonstrated that cRGD modification significantly enhanced nanoparticle uptake by ADP-activated platelets, with nanoparticles containing 40% PLGA-PEG-cRGD in the total PLGA-methoxy PEG (mPEG) formulation showing the strongest uptake (Figure S2D). Therefore, a 2:3 PLGA-PEG-cRGD:PLGA-mPEG ratio was used to prepare cRGD-NP@A (Figure 1A). Transmission electron microscopy (TEM) revealed a spherical shape of cRGD-NP@A with a hydrodynamic diameter of ~104 nm (Figures 1B and 1C; Table S1). The drug loading rate and encapsulation efficiency of cRGD-NP@A were 5.58% ± 0.17% and 59.10% ± 1.92%, respectively (Table S1), with a markedly higher *in vitro* drug release rate at pH 5.0 (57%) than that at pH 7.4 (18%) within 48 h (Figure 1D). The hydrodynamic size of cRGD-NP@A did not change obviously when incubated with 10% fetal bovine serum for 24 h at 37°C or stored at 4°C for 7 days (Figures S5A and S5B), suggesting excellent stability of the nanoparticles. The hemolytic activity assay revealed no significant hemolysis induced by cRGD-NP@A, indicating its favorable biocompatibility (Figure S5C).

cRGD-NP@A binding to TAPs triggers apoptosis of TAPs *in vitro*

The targeting capability of cRGD-NP@A toward activated platelets was first evaluated *in vitro*, using unmodified nanoparticles (PEG-NP@A) as the control. Flow cytometry analysis demonstrated a 3.7-fold increase in Cy5.5 fluorescence in ADP-activated platelets incubated with Cy5.5-labeled cRGD-NP@A, compared to PEG-NP@A (Figures 2A and S6A). By contrast, comparable Cy5.5 fluorescence levels were detected in resting platelets treated with PEG-NP@A or cRGD-NP@A. Consistently, confocal microscopy observations revealed a faster and increased accumulation of cRGD-NP@A in activated platelets compared to resting platelets (Figure S6B). Blocking GPIIb/IIIa receptors with fibrinogen or cRGD significantly reduced the

uptake of cRGD-NP@A by activated platelets to levels comparable to PEG-NP@A, whereas blocking integrin β1 on platelets showed no detectable effect on cRGD-NP@A uptake (Figure S6C). In contrast, neutrophils, monocytes, B cells, and T cells, which express various integrins such as $\alpha_L\beta_2$ and $\alpha_4\beta_1$, demonstrated comparable uptake for both cRGD-modified and unmodified nanoparticles (Figure S6D). These results further suggest that cRGD facilitates nanoparticle entry specifically by binding to GPIIb/IIIa receptors on activated platelets. The activated platelet apoptosis was then measured by flow cytometric determination of mitochondrial membrane potential ($\Delta\Psi m$) dissipation and phosphatidylserine (PS) externalization. Treatment with cRGD-NP@A for 2 h triggered a significantly enhanced apoptotic response in ADP-activated platelets than in resting platelets, as evidenced by the higher percentages of $\Delta\Psi m$ depolarization and stronger PS fluorescence signals detected in the former (Figures 2B and 2C). Western blot analysis of apoptosis-related proteins in activated platelets revealed that both cRGD-NP@A and free ABT-737 shared similar mechanisms of action, marked by reduced levels of anti-apoptotic B-cell lymphoma-extra large protein (BCL-xL) and increased caspase-3 expression (Figures S7A–S7C). Treatment with cRGD peptide or empty cRGD-NP nanoparticles did not induce significant PS exposure in either resting or activated platelets (Figure S8A). Besides, treatment with cRGD peptide or cRGD-NP@A for 2 h failed to trigger significant apoptosis in B16-F10 cells even at ABT-737 concentrations up to 10 μM (Figure S8B), possibly due to the limited binding of cRGD to these cells and the intrinsic resistance of B16-F10 cells to ABT-737-induced apoptosis.[29,38] These findings suggest that cRGD modification enhances the uptake of cRGD-NP@A by activated platelets, facilitating subsequent apoptosis through the release of ABT-737 within the platelets.

We then examined the targeting and apoptosis-inducing capabilities of cRGD-NP@A in TAPs, prepared by exposing platelets to adherent B16-F10 tumor cells, which were removed after co-incubation. cRGD-NP@A displayed rapid accumulation within tumor cell-stimulated platelets, with a robust Cy5.5 fluorescence signal observed using confocal microscopy (Figure 2D). Minimal Cy5.5 fluorescence signal was detected in TAPs treated with PEG-NP@A or in resting platelets treated with either nanoparticle, indicating the excellent TAP targeting ability of cRGD-NP@A. We further compared the apoptosis-inducing efficiency of cRGD-NP@A in TAPs and resting platelets. Both free ABT-737 and PEG-NP@A triggered comparable levels of apoptosis in platelets with and without B16-F10 stimulation, with both relative apoptotic rates (represented as TAPs normalized to resting platelets) being ~1 (Figures 2E and 2F). In contrast, cRGD-NP@A induced a 2- to 3-fold higher $\Delta\Psi m$ depolarization and PS externalization in TAPs compared to resting platelets. These data demonstrate that cRGD-NP@A effectively targets TAPs and induces apoptosis more efficiently than in resting platelets. This differential activity could be crucial for selectively eliminating hyperreactive TAPs *in vivo*.

cRGD-NP@A accumulates in TAPs to inhibit platelet-tumor cell interaction *in vivo*

We first analyzed the biodistribution and pharmacokinetics of cRGD-NP@A by measuring plasma and tissue drug concentrations at various time points following single intravenous administration in healthy C57BL/6N mice. The results showed that cRGD-NP@A was predominantly metabolized by the liver, with most of the drug cleared within 24 h, suggesting a low risk of accumulation-related toxicity (Figure S9). The TAP targeting ability of cRGD-NP@A was then evaluated in B16-F10 metastasis-bearing mice following intravenous injection of free Cy5, Cy5-labeled PEG-NP@A, and cRGD-NP@A. *In vivo* real-time fluorescence imaging showed higher Cy5 fluorescence in the lung region of mice treated with cRGD-NP@A compared to control groups within 24 h post injection (Figure S10A). *Ex vivo* imaging of major organs revealed a 5-fold and 4-fold increase of Cy5 fluorescence in the lungs of mice after cRGD-NP@A treatment compared to those treated with free Cy5 and PEG-NP@A, respectively (Figures 3A and 3B). In contrast, the cRGD-NP@A and PEG-NP@A exhibited similar biodistribution in healthy C57BL/6N mice, with comparable fluorescence intensities observed in the lungs and other major organs (Figures S10B–S10D). Furthermore, the lungs of mice collected 2 h post treatment with cRGD-NP@A showed significantly stronger Cy5 fluorescence compared to those treated with PEG-NP@A, with clear colocalization between platelets (CD41 staining) and nanoparticles in metastatic foci (Figure 3C). These findings suggest that cRGD-NP@A effectively targets TAPs *in vivo*, leading to increased accumulation within the pulmonary metastasis regions.

Then, we investigated the apoptosis-inducing effects of cRGD-NP@A *in vivo*. Flow cytometry analysis of PS exposure on circulating platelets from B16-F10 lung metastasis-bearing mice treated with cRGD-NP@A revealed significant apoptosis in $CD62P^+$ platelets, while resting platelets remained unaffected (Figure S11A). In contrast, free ABT-737 triggered strong apoptotic responses in both resting and activated platelets. The abundant PS on the surface of TAPs facilitates their recognition and clearance by phagocytes, thereby preventing TAPs from further interacting with tumor cells and promoting metastasis. We then proceeded to investigate the influence of cRGD-NP@A treatment on *in vivo* platelet-tumor cell interactions. We first tested whether cRGD-NP@A could inhibit the formation of circulating tumor cell-platelet hetero-aggregates. Immunofluorescence analysis of lung tissue sections from mice co-injected with FITC-anti-CD41 antibody (for platelet labeling) and CellMask Orange-labeled B16-F10 cells showed significant platelet adherence and aggregation in the vicinity of B16-F10 cells, which was partially inhibited by free ABT-737 and almost completely suppressed by cRGD-NP@A (Figures 3D and S11B). Furthermore, B16-F10 lung metastasis-bearing mice treated with cRGD-NP@A for three consecutive treatments showed significantly decreased platelet surface CD62P and active GPIIb/IIIa expression, indicating the effective inhibition of tumor cell-induced platelet activation by cRGD-NP@A *in vivo* (Figures 3E and S11C). In contrast, free ABT-737-treated mice exhibited similar platelet activation levels to saline-treated controls, likely due to the lack of TAP selectivity. Considering the critical role of platelets in coagulation, we evaluated the impact of cRGD-NP@A treatment on the coagulation function of metastasis-bearing mice. In comparison to normal and saline-treated controls, mice treated with free ABT-737 exhibited a significant decrease in platelet count, prolonged tail bleeding time, and an increase in activated

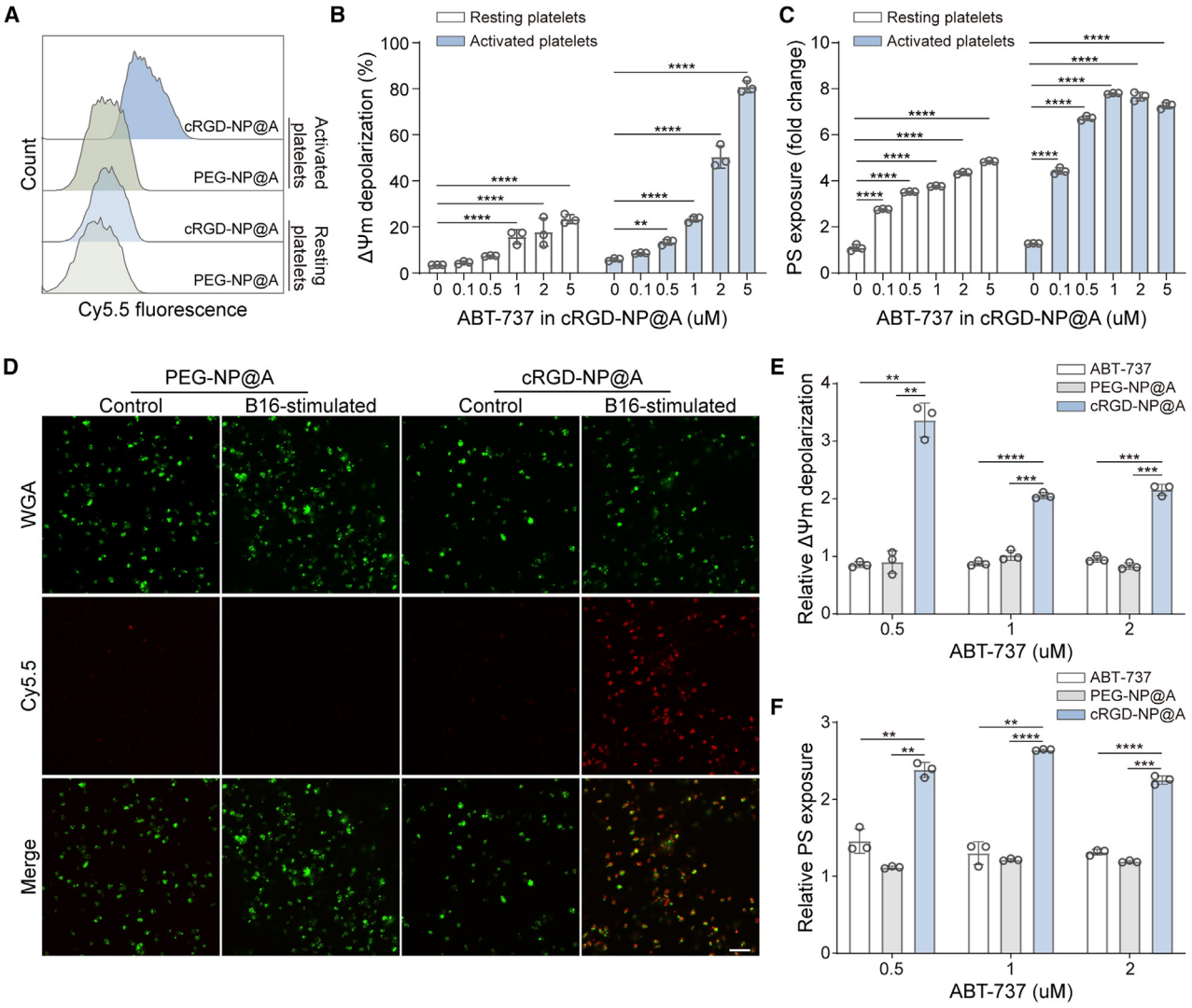

Figure 2. cRGD-NP@A binding to TAPs triggers their apoptosis *in vitro*

(A) Flow cytometry analysis of Cy5.5 fluorescence signals of resting or activated platelets after incubation with Cy5.5-labeled PEG-NP@A or cRGD-NP@A for 30 min, respectively.

(B and C) Measurement of mitochondrial membrane potential (ΔΨm) depolarization (B) and PS externalization (C, presented as annexin V fluorescence fold change normalized to resting platelets without cRGD-NP@A treatment) in resting or ADP-activated platelets following treatment with cRGD-NP@A for 2 h.

(D) Representative confocal microscopy images of B16-F10-stimulated or unstimulated platelets after incubation with Cy5.5-labeled PEG-NP@A or cRGD-NP@A for 10 min, respectively. Scale bar, 10 μm.

(E and F) Measurement of ΔΨm depolarization (E) and PS externalization (F) in resting or B16-F10-stimulated platelets after treatment with free ABT-737, PEG-NP@A, or cRGD-NP@A, respectively. Data are presented as relative apoptotic rates of B16-F10-stimulated platelets normalized to unstimulated controls after treatment with the same concentration of ABT-737 in different formulations.

Values are mean ± SD, $n = 3$ biological replicates. Statistical significance was analyzed using two-way ANOVA followed by Dunnett's test. $^{*}p < 0.05$, $^{**}p < 0.01$, $^{***}p < 0.001$, $^{****}p < 0.0001$.

See also Figures S6–S8.

partial thromboplastin time (APTT), indicating impaired coagulation function (Figures S12A–S12C). Intriguingly, treatment with cRGD-NP@A restored the tail bleeding time and APTT to levels comparable to those of normal mice, suggesting an amelioration of the hypercoagulable state. Furthermore, platelet count, prothrombin time, thrombin time, and fibrinogen concentration were also similar between cRGD-NP@A-treated mice and normal controls (Figures S12D–S12F). Taken together, these data suggest that cRGD-NP@A effectively targets TAPs and disrupts the interaction between platelets and tumor cells *in vivo*. This disruption exposes circulating tumor cells and reduces tumor-induced platelet activation, thereby alleviating systemic hypercoagulability associated with metastatic tumors and offering an effective approach to managing cancer-associated thrombosis.

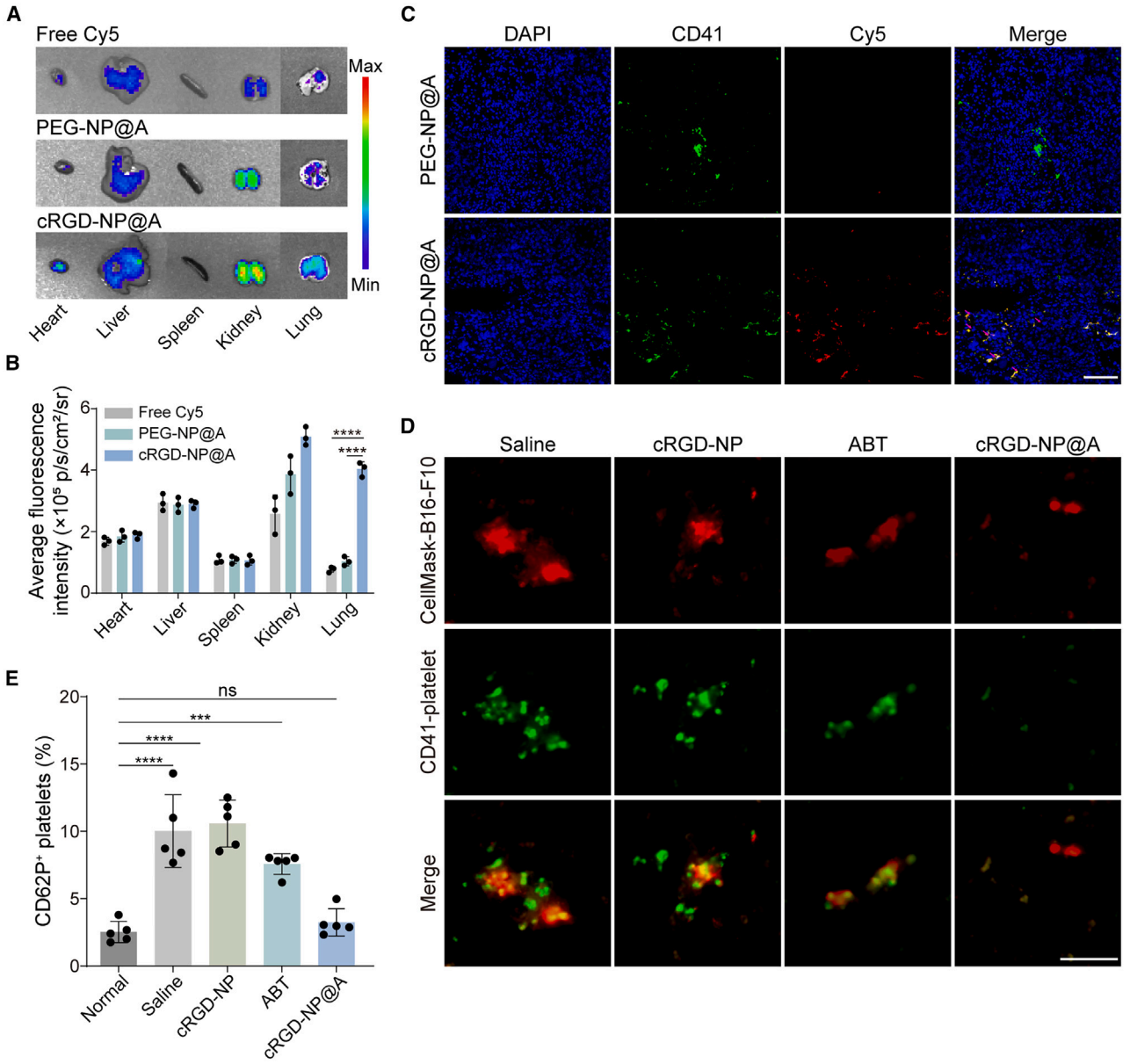

Figure 3. cRGD-NP@A accumulates in TAPs to inhibit platelet-tumor cell interaction *in vivo*

(A and B) *Ex vivo* fluorescence imaging (A) and average Cy5 fluorescence intensity (B) of major organs harvested from C57BL/6N mice bearing B16-F10 pulmonary metastasis at 24 h after intravenous injection of free Cy5, Cy5-labeled PEG-NP@A, or cRGD-NP@A (n = 3 mice per group).

(C) Immunofluorescence analysis of cRGD-NP@A distribution within metastatic foci 2 h post injection of Cy5-labeled PEG-NP@A or cRGD-NP@A. CD41 staining was used to visualize platelets. Scale bar, 100 μm.

(D) Analysis of platelet adherence to B16-F10 tumor cells *in vivo*. Lungs from healthy C57BL/6N mice treated with various formulations, following co-injection of CellMask Orange-labeled B16-F10 cells and FITC-anti-CD41 antibody, were harvested for frozen section analysis. Scale bar, 50 μm.

(E) Determination of circulating platelet activation level in B16-F10 lung metastasis-bearing mice after three treatments with saline, cRGD-NP, free ABT-737, and cRGD-NP@A, respectively, at an interval of three days (n = 5 mice per group).

Data are presented as mean ± SD. Statistical significance was analyzed using two-way (B) or one-way (E) ANOVA with Dunnett's test. ***$p < 0.001$, ****$p < 0.0001$; ns, not significant.

See also Figures S9–S12.

cRGD-NP@A enhances anti-metastatic effects of aPD-1 therapy by augmenting anti-tumor immune response

We proceeded to explore whether cRGD-NP@A-mediated TAP elimination could inhibit tumor metastasis formation and enhance immune activation, thus augmenting the anti-metastatic efficacy of aPD-1 (Figure 4A). The anti-metastatic activity of cRGD-NP@A and its influence on aPD-1 efficacy was first evaluated in C57BL/6N mice bearing B16-F10 lung metastases. Six

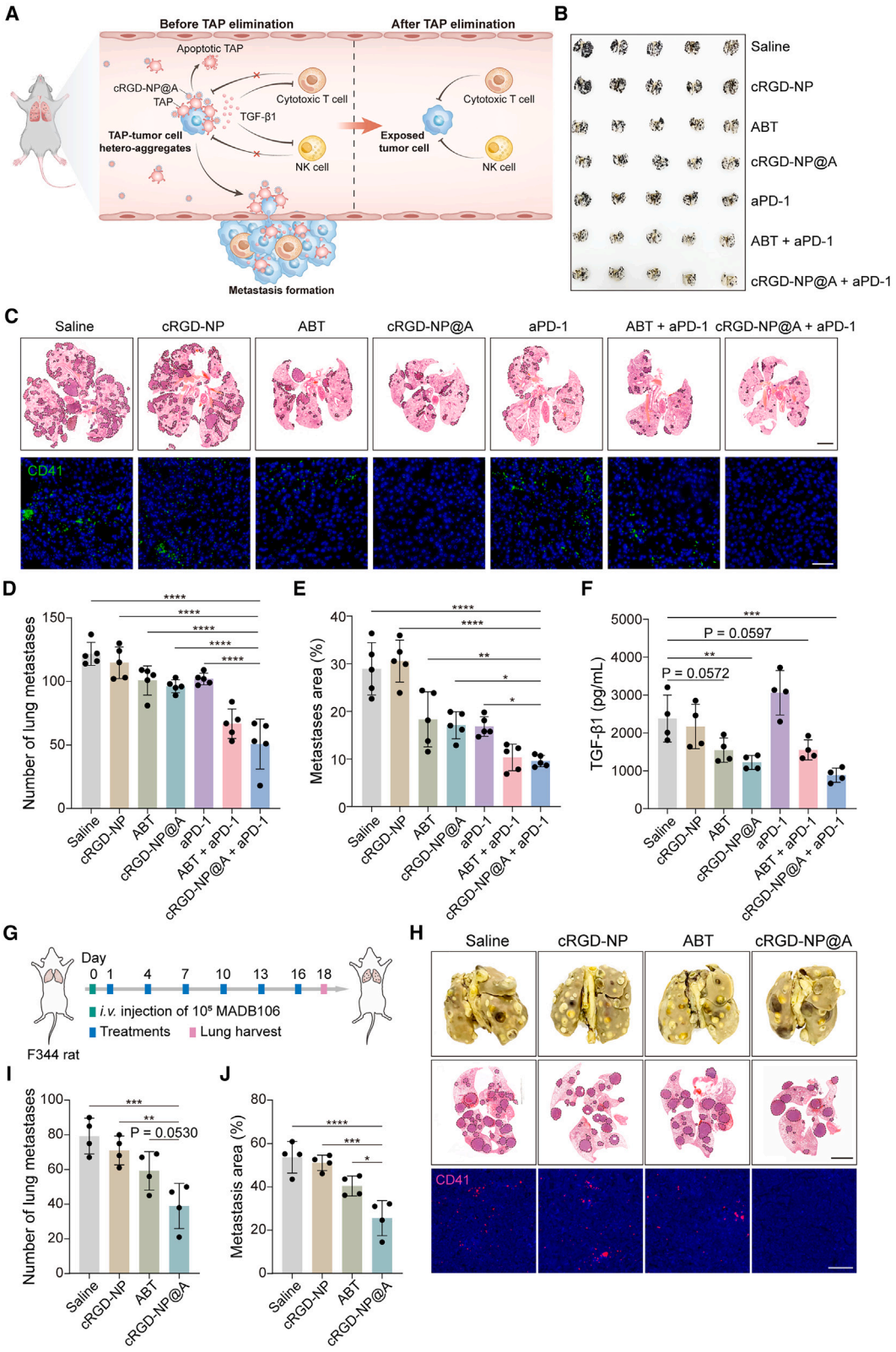

(legend on next page)

treatments with cRGD-NP@A or aPD-1 resulted in a similar reduction in lung surface metastatic nodules (~20% reduction) and metastatic areas (~40% reduction) compared with the saline group (Figures 4B–4E). In contrast, the combination of cRGD-NP@A with aPD-1 led to a remarkably enhanced anti-metastatic effect, reducing the number of lung metastases by 58% and causing a 67% reduction in the metastatic area. Correspondingly, treatment with the combination of cRGD-NP@A and aPD-1 resulted in the greatest extension of survival in B16-F10 metastasis-bearing mice compared to other control groups. The median survival times were 20.5, 22, 24.5, and 29 days for the saline, cRGD-NP@A, aPD-1, and the cRGD-NP@A and aPD-1 combination groups, respectively (Figure S13). Furthermore, no obvious TAP infiltration in lung metastatic sites was detected in mice treated with cRGD-NP@A or cRGD-NP@A plus aPD-1, and the circulating TGF-β1 level was also significantly decreased in both groups in contrast to saline-treated controls, indicating that cRGD-NP@A efficiently induced TAP elimination and blocked the secretion of TGF-β1 (Figures 4C and 4F). These findings demonstrate that the efficient elimination of TAPs by cRGD-NP@A exerts a noticeable anti-metastatic effect, and combining cRGD-NP@A with aPD-1 substantially boosts the anti-metastatic efficacy of aPD-1 therapy.

We further validated the impact of cRGD-NP@A treatment on aPD-1 efficacy in a C57BL/6N mouse model bearing LLC Lewis lung carcinoma pulmonary metastasis (Figure S14A). This model was selected due to the significant application of PD-1 blockade therapy and the relatively high incidence of metastasis in lung cancer. Six treatments with cRGD-NP@A led to a smaller number of lung metastatic nodules (~30% reduction) and a reduced metastatic area (~44% reduction) compared with the saline group (Figures S14B–S14D). Treatment with aPD-1 alone exhibited minimal anti-metastatic effect, while the combination of cRGD-NP@A with aPD-1 dramatically improved the therapeutic effectiveness of aPD-1, resulting in the fewest nodules and the smallest metastatic area in the lungs. Further staining of CD41 for platelets confirmed the effective elimination of TAPs in metastatic foci in mice treated with cRGD-NP@A or cRGD-NP@A plus aPD-1 (Figure S14B, lower panel). Next, we extended our investigation to evaluate the broader applicability of cRGD-NP@A for anti-metastasis therapy in a rat pulmonary metastasis model established by tail vein injection of MADB106 rat breast cancer cells (Figure 4G). After six intravenous administrations, the number of lung metastases and lung metastatic area were significantly reduced in rats treated with cRGD-NP@A in contrast to various controls, with minimal infiltration of platelets observed in metastatic foci (Figures 4H–4J). Although there is currently no aPD-1 antibody available for *in vivo* administration in rats, the observed effective elimination of TAPs and anti-metastatic activity of cRGD-NP@A suggest its potential applicability for inhibiting metastasis and enhancing the response to aPD-1 therapy. To evaluate the translational potential of cRGD-NP@A as an anti-metastatic strategy, a patient-derived metastatic model was established in BALB/c nude mice via intravenous injection of bladder cancer patient-derived tumor cells, with subsequent immunohistochemistry confirming high GATA3 (a urothelial marker) expression in both the original patient tumor and mouse metastases (Figure S15A), indicating well-preserved pathological characteristics of the model. Seven consecutive administrations of cRGD-NP@A resulted in approximately 56% and 44% reductions in the number and area of lung metastases, respectively (Figures S15B and S15C). Additionally, *in vitro* co-culture experiments involving bladder cancer patient-derived peripheral blood mononuclear cells (PBMCs), platelets, and tumor cells demonstrated a significant attenuation of PBMC-mediated cytotoxicity against tumor cells due to the presence of platelets in the context of aPD-1 treatment (Figure S15D). However, the addition of cRGD-NP@A markedly restored PBMC functionality, yielding an apoptotic response in tumor cells comparable to that observed in the absence of platelets. These findings underscore the efficacy of our TAP-targeting nanomedicine and its potential for improving outcomes in patients with metastatic cancer by enhancing the effectiveness of PD-1 blockade therapy. Overall, cRGD-NP@A exhibits strong anti-metastatic properties via selectively eliminating TAPs across various experimental metastasis models in mice and rats. Notably, when combined with aPD-1, cRGD-NP@A significantly boosts the effectiveness of the treatment, highlighting its potential to enhance clinical outcomes for patients with metastatic cancer receiving aPD-1 therapy.

Figure 4. cRGD-NP@A enhances anti-metastatic effects of aPD-1 therapy

(A) Schematic illustration of the action mechanisms of cRGD-NP@A. Intravenous administration of cRGD-NP@A specifically targets TAPs in the circulation and metastatic sites. cRGD-NP@A then induces apoptosis in TAPs upon endocytosis, thereby exposing tumor cells to immune cell recognition and killing. This intervention simultaneously suppresses the secretion of TGF-β1 by TAPs, further activating immune response. Ultimately, these actions potentiate the anti-metastatic effects of concurrent aPD-1 therapy.

(B) Image of lungs collected from B16-F10 metastasis-bearing mice after different treatments.

(C) H&E (upper) analysis and CD41 immunofluorescence staining (lower) of lung tissue sections from mice bearing B16-F10 pulmonary metastasis. Scale bar, 2 mm for the upper panel, 50 μm for the lower panel.

(D and E) Number of surface nodules (D) and metastatic area quantification (E, metastasis region/total region) of lungs harvested from B16-F10 metastasis-bearing mice (n = 5 mice per group).

(F) Plasma level of TGF-β1 of B16-F10 lung metastasis-bearing mice after different treatments (n = 4 mice per group).

(G) Treatment schedule for anti-metastasis evaluation in F344 rats bearing MADB106 pulmonary metastasis.

(H) Representative images (upper), H&E analysis (middle), and CD41 staining (lower) of lung sections from rats bearing MADB106 metastasis. Scale bars, 5 mm for the middle panel, 100 μm for the lower panel.

(I and J) Number of surface metastatic nodules (I) and metastatic area quantification (J) of lungs from MADB106 metastasis-bearing rats after different treatments. n = 4 rats for each group.

Values are mean ± SD. Statistical significance was determined by one-way ANOVA with Dunnett's test. *$p < 0.05$, **$p < 0.01$, ***$p < 0.001$, ****$p < 0.0001$.

See also Figures S13–S15.

CellPress
OPEN ACCESS

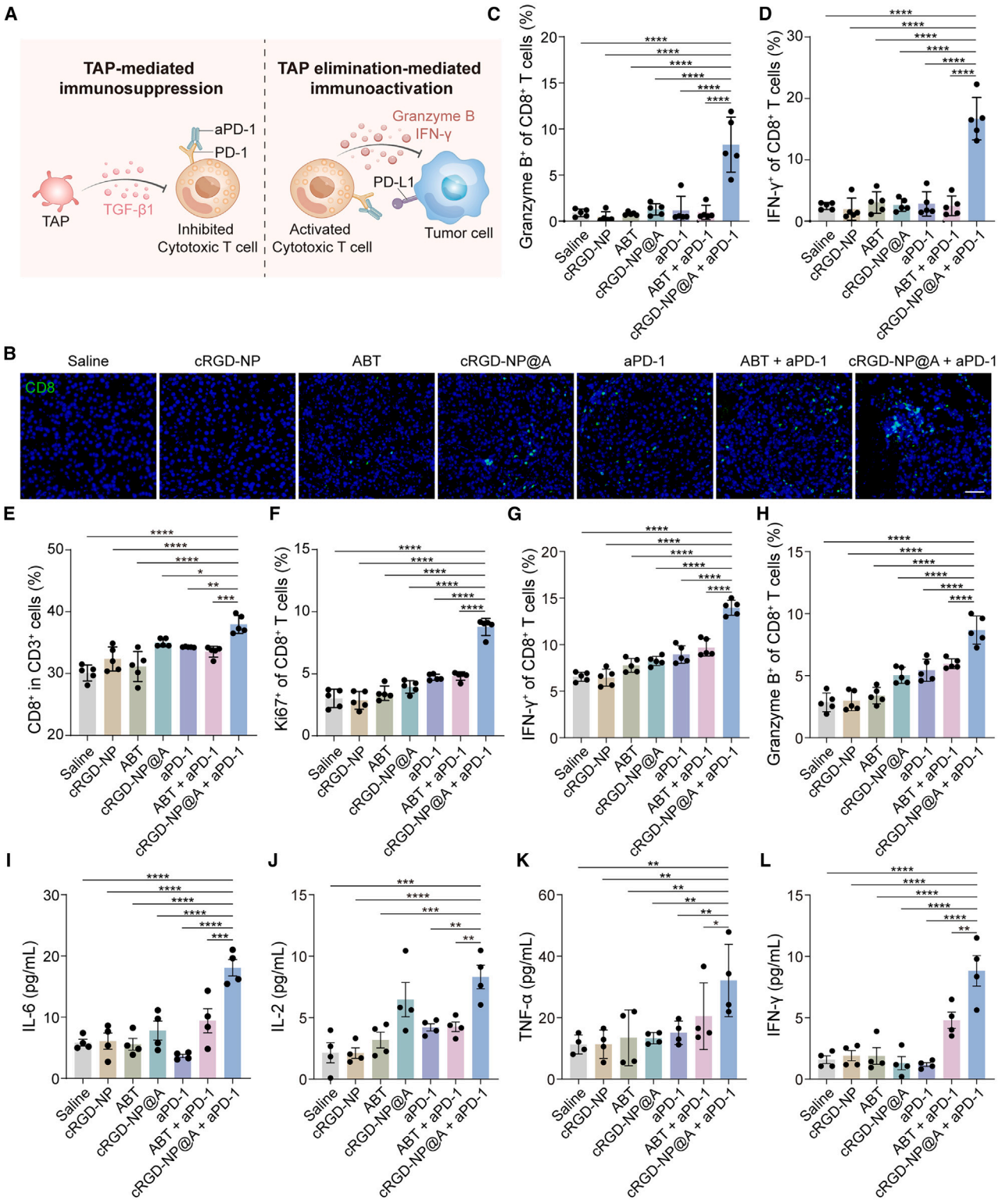

Figure 5. cRGD-NP@A augments cytotoxic T cell response of aPD-1 therapy

(A) Schematic illustration of cRGD-NP@A enhancing CTL response to aPD-1 therapy by depleting TAPs for blocking TGF-β1-mediated immunosuppression.

(B) Immunofluorescence analysis of CD8⁺ T cell infiltration in B16-F10 pulmonary metastatic foci. Scale bar, 50 μm.

(legend continued on next page)

Then, we initiated preliminary investigations to elucidate the mechanism underlying the enhancement of aPD-1 therapy by cRGD-NP@A. TGF-β1 is a key immunosuppressive factor in tumors that inhibits the function of anti-tumor immune cells such as natural killer (NK) cells, dendritic cells (DCs), and cytotoxic T lymphocytes (CTLs), while promoting the expansion of regulatory T cells (Tregs). We hypothesized that reduced TGF-β1 secretion resulted from cRGD-NP@A treatment could reactivate systemic anti-tumor immunity and enhance aPD-1-mediated immune responses (Figure 5A). To test this hypothesis, we comprehensively analyzed major immune cell populations in mice bearing B16-F10 lung metastasis at the end of the treatment. In line with the findings from the anti-metastasis assessment, mice receiving cRGD-NP@A plus aPD-1 treatment displayed the highest infiltration of CTLs ($CD8^+$ T cells) and the lowest presence of $FOXP3^+$ Tregs within the metastatic foci compared with mice treated with other controls (Figures 5B and S16A). Flow cytometry analysis of the peripheral blood lymphocytes revealed the highest frequencies of interferon-gamma (IFN-γ)- and granzyme B-secreting $CD3^+CD8^+$ T cells in mice treated with cRGD-NP@A plus aPD-1 (Figures 5C and 5D). Conversely, mice treated with aPD-1 alone showed no significant differences in peripheral $CD8^+$ T cell activation compared to the saline group, suggesting a limited immune response to aPD-1 treatment. In mice treated with cRGD-NP@A, either alone or in combination with aPD-1, analysis of CD80 and CD86 expression on DCs in peripheral blood showed a significant increase in DC maturation compared to the saline group (Figure S16B). Likewise, the cRGD-NP@A-treated groups exhibited a marked upregulation of the natural killer group 2 member D (NKG2D) activating receptor and the degranulation marker CD107a, indicating enhanced NK cell function (Figure S16C). Additionally, the proportion of $CD4^+FOXP3^+$ Tregs in the blood was significantly reduced following cRGD-NP@A treatment (Figure S16D). In contrast, aPD-1 treatment alone produced a limited response in these immune cells, likely due to the high levels of circulating TGF-β1. Moreover, analysis of splenocytes also showed the highest proportion of $CD3^+CD8^+$ T cells in mice treated with cRGD-NP@A plus aPD-1 (Figure 5E). Further examination of $CD3^+CD8^+$ T cell status revealed limited CTL activation following aPD-1 treatment, whereas the combination of cRGD-NP@A with aPD-1 markedly enhanced the systemic immune response, with the highest rates of proliferated ($Ki67^+$), IFN-γ-, and granzyme B-secreting $CD3^+CD8^+$ T cells in the spleen (Figures 5F–5H). In addition, the serum levels of representative inflammatory cytokines (interleukin [IL]-6, IL-2, tumor necrosis factor alpha [TNF-α], and IFN-γ), important for anti-tumor immunity, were significantly elevated in mice treated with cRGD-NP@A plus aPD-1 in contrast to various controls (Figures 5I–5L). Furthermore, the combination of cRGD-NP@A and aPD-1 did not induce such immune responses in healthy C57BL/6N mice following three consecutive treatments. Levels of IFN-γ- and granzyme B-secreting $CD3^+CD8^+$ T cells, as well as $CD4^+FOXP3^+$ Tregs in peripheral blood, were minimal and comparable to those in the saline-treated group (Figures S17A–S17C), indicating that the immune regulatory functions remained largely intact. Collectively, these findings underscore the limited immune response to aPD-1 treatment alone, potentially explaining its suboptimal anti-metastatic efficacy. However, combining cRGD-NP@A with aPD-1 significantly enhances the immune response by eliminating TAPs and reducing immunosuppressive factor secretion.

Reduction of TGF-β1 level mediates the immune-enhancing effects of cRGD-NP@A on aPD-1 therapy

The ability of cRGD-NP@A to reduce circulating TGF-β1 levels and enhance aPD-1-mediated immune responses prompted further investigation into the role of TGF-β1 in cRGD-NP@A potentiation of aPD-1 therapy. Initially, we evaluated the impact of TGF-β1 on the anti-metastatic efficacy of cRGD-NP@A and aPD-1 combination therapy in the B16-F10 lung metastasis model. Recombinant TGF-β1 (rTGF-β1) significantly diminished the anti-metastatic efficacy of the combination treatment, increasing the number of metastases from 19 to 49, comparable to aPD-1 monotherapy (Figures 6A and 6B). Conversely, combining aPD-1 with SB-431542, a TGF-β receptor kinase inhibitor, significantly enhanced the anti-metastatic efficacy, resulting in fewer metastases compared to the aPD-1 group. These findings underscore the critical role of TGF-β1 signaling in limiting the therapeutic effectiveness of PD-1 blockade therapy and highlight its contribution to the aPD-1 enhancement by cRGD-NP@A. To explore the underlying mechanisms, we further investigated the impact of TGF-β1 on immune activation triggered by the combination of cRGD-NP@A and aPD-1. In peripheral blood, supplementation with rTGF-β1 in cRGD-NP@A/aPD-1 combination-treated mice resulted in a notable increase in the proportion of $CD4^+FOXP3^+$ Tregs, reduced CD80 and CD86 expression on DCs, impaired NK cell activation and degranulation, and decreased secretion of IFN-γ and granzyme B by CTLs (Figures 6C–6F). In contrast, the combination of aPD-1 with SB-431542 significantly reduced $CD4^+$ Tregs in circulation, upregulated NKG2D on NKs and CD86 on DCs, and enhanced granzyme B secretion by CTLs compared to aPD-1 monotherapy. Similarly, in the spleen, rTGF-β1 combined with cRGD-NP@A and aPD-1 led to a significant decrease in CTL production of IFN-γ and granzyme B compared to the group treated with cRGD-NP@A plus aPD-1, whereas SB-431542 treatment enhanced granzyme B production by CTLs in the spleen induced

(C and D) Flow cytometry analysis of granzyme B (C) and IFN-γ (D) secretion by $CD3^+CD8^+$ T cells in peripheral blood from B16-F10 metastasis-bearing mice at the end of treatment. $n = 5$ mice for each group.

(E–H) Proportions of $CD3^+CD8^+$ T cells in lymphocytes (E), and $Ki67^+$ (F), IFN-γ^+ (G), and granzyme B^+ (H) $CD3^+CD8^+$ T cells in the spleen from B16-F10 metastasis-bearing mice following various treatments. $n = 5$ mice for each group.

(I–L) Serum levels of major pro-inflammatory cytokines in B16-F10 lung metastasis-bearing mice after different treatments. $n = 4$ mice for each group.

Data are presented as mean ± SD. Statistical significance was determined by one-way ANOVA with Dunnett's test. $^*p < 0.05$, $^{**}p < 0.01$, $^{***}p < 0.001$, $^{****}p < 0.0001$.

See also Figures S16 and S17.

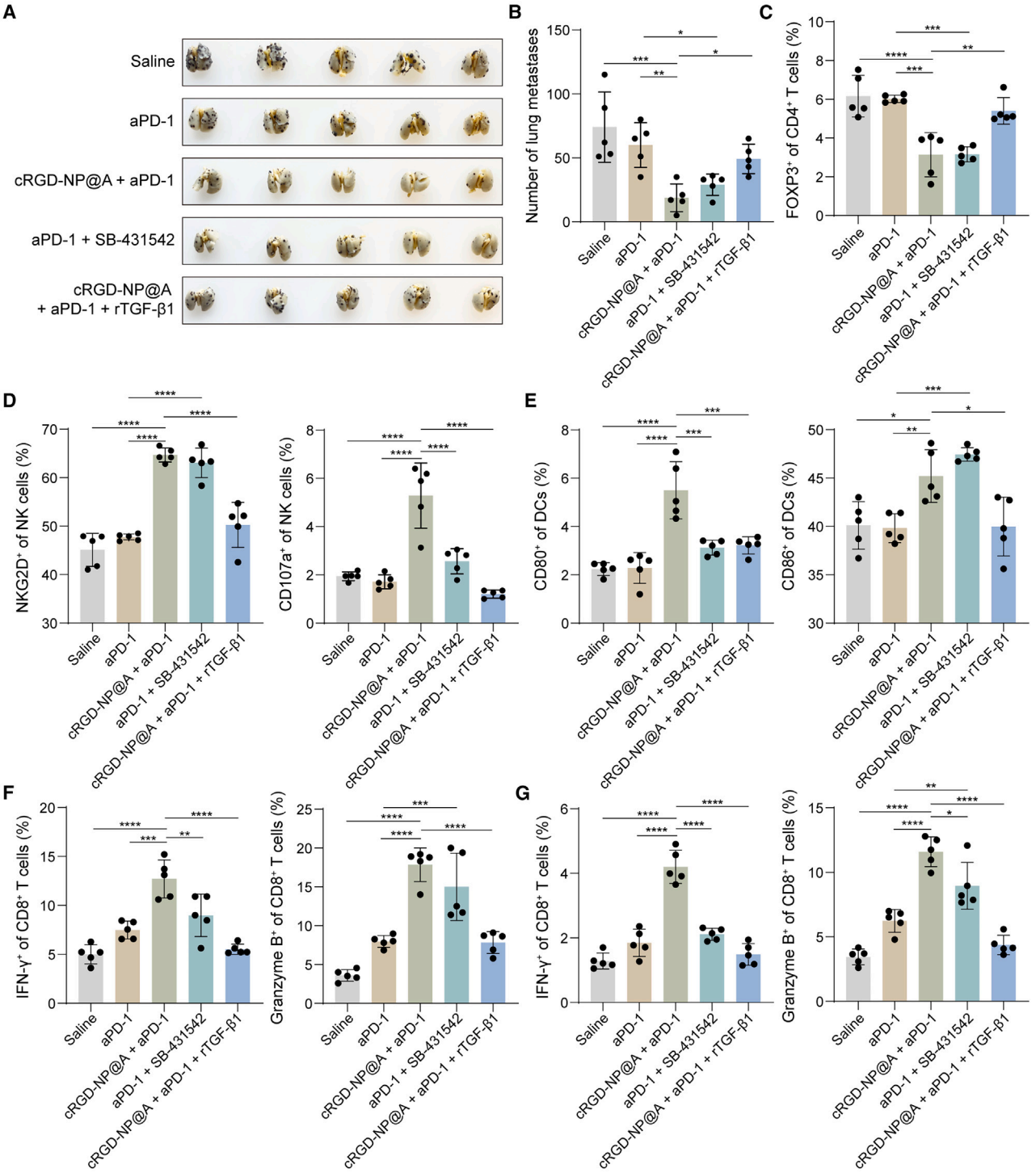

Figure 6. Reduction of TGF-β1 level mediates the immune-enhancing effects of cRGD-NP@A on aPD-1 therapy

(A) Image of lungs collected from B16-F10 metastasis-bearing mice after different treatments.

(B) Number of surface nodules of lungs harvested from B16-F10 metastasis-bearing mice after different treatments.

(C) Flow cytometry analysis of the proportion of $CD4^+FOXP3^+$ Tregs in peripheral blood from B16-F10 metastasis-bearing mice at the end of the experiment.

(legend continued on next page)

by aPD-1 therapy (Figure 6G). These results demonstrate that through disrupting platelet-tumor cell interaction, our cRGD-NP@A reduces TGF-β1 secretion by hyperactive TAPs, leading to an improved tumor immune microenvironment and restoration of anti-tumor immune cell function, thereby enhancing the immune responses induced by aPD-1 therapy.

Combination of cRGD-NP@A with aPD-1 treatment does not cause cumulative toxicity

We first conducted a comprehensive investigation into the effects of cRGD-NP@A on platelet function. Within the concentration range of 0.1–10 μM, 2-h *in vitro* treatment with cRGD-NP@A had a minimal impact on platelet adhesion to collagen and activation in response to ADP stimulation (Figures S18A and S18B). While a modest inhibition of platelet aggregation was observed at 1–10 μM, it was significantly weaker than that of free ABT-737, which substantially inhibited both platelet activation and aggregation even at a lower concentration of 0.1 μM (Figure S18C). Additionally, given the complex roles of platelets as immune-regulatory cells, both pro- and anti-inflammatory,[27,28] we assessed the impact of cRGD-NP@A on platelet-mediated immune regulation by examining the responses of healthy C57BL/6N mice to lipopolysaccharide stimulation after three consecutive treatments with cRGD-NP@A. Plasma levels of key inflammatory cytokines, TNF-α and IL-6, in cRGD-NP@A-treated mice, were comparable to those in the saline-treated group. In contrast, free ABT-737 treatment resulted in a slight increase in IL-6 (Figure S18D), likely due to impaired immune regulation caused by non-specific platelet toxicity. These results emphasize the advantage of targeted ABT-737 delivery to hyperactive/activated platelets, minimizing systemic platelet interference.

To evaluate the potential unintended effects of cRGD-NP@A on circulating cells, particularly leukocytes, we assessed the uptake of Cy5-labeled cRGD-NP@A by $CD45^+$ immune cells isolated from healthy C57BL/6N mice 2 h post injection. Flow cytometry analysis revealed minimal nanoparticle internalization, with fewer than 1% of $CD45^+$ cells exhibiting Cy5 fluorescence (Figure S19A). Moreover, treatment with cRGD-NP@A did not result in significant apoptosis in circulating neutrophils, monocytes, and B and T cells (Figure S19B). The counts and proportions of these immune cells, along with the total white blood cell count, remained unchanged in B16-F10 metastasis-bearing mice after six consecutive cRGD-NP@A treatments (Figures S19C–S19E). These results indicate that cRGD-NP@A has negligible interaction with circulating leukocytes, supporting its targeted action and demonstrating a favorable safety profile *in vivo*. Given that GPIIb/IIIa (the CD41/CD61 complex) is also expressed on megakaryocytes and certain hematopoietic stem cells, we further investigated the impact of cRGD-NP@A on these cells. Flow cytometry analysis demonstrated no significant uptake of Cy5-labeled cRGD-NP@A by $CD41^+$ cells isolated from the bone marrow of healthy C57BL/6N mice, 6 h after intravenous injection, with comparable Cy5 fluorescence and PS exposure between the saline- and cRGD-NP@A-treated groups (Figures S20A and S20B). These findings suggest that cRGD-NP@A has minimal effects on megakaryocytes or other GPIIb/IIIa$^+$ cells, likely due to limited nanoparticle accessibility to these cell populations.

Administration of cRGD-NP@A or cRGD-NP@A plus aPD-1 did not cause significant body weight loss in mice or rats bearing pulmonary metastases during the whole anti-metastasis experiments (Figures S21A–S21C), indicating the favorable biocompatibility of cRGD-NP@A and its combination with aPD-1 treatment. Detailed blood tests, including analysis of whole blood routine and serum biochemical parameters for heart, liver, and kidney function assessment, were also conducted in rats at the end of the anti-metastasis experiment following six treatments of cRGD-NP@A. No abnormalities were detected in these parameters in rats treated with cRGD-NP@A, while treatment with free ABT-737 notably reduced platelet count, likely attributed to undesired toxicity in resting platelets (Figures S22A–S22J). TUNEL analysis of other major organs harvested from B16-F10 metastasis-bearing mice at the end of the anti-metastasis experiment revealed no noticeable cell apoptosis in the heart, liver, spleen, and kidney following treatment with cRGD-NP@A, either alone or in combination with aPD-1 (Figure S23). The biosafety of combining cRGD-NP@A with aPD-1 was further investigated in healthy C57BL/6N mice after six treatments. No significant increases in major serum biochemical indicators were observed following treatment with cRGD-NP@A alone or in combination with aPD-1 (Figures S24A–S24F). Additionally, hematoxylin and eosin (H&E) staining revealed no apparent histological damage in major organs, including the heart, liver, spleen, lung, and kidney (Figure S24G). These results collectively demonstrate the favorable biosafety profile of cRGD-NP@A and indicate that its combination with aPD-1 does not induce cumulative toxicity in mice.

DISCUSSION

Despite significant advances in treating advanced cancers with immune checkpoint blockade therapy, limited response rates and efficacy continue to pose substantial challenges in clinical practice. It has been shown that tumors can modify both the count and function of platelets to support tumor growth and metastasis.[9,39] When tumor cells circulate in the bloodstream, TAPs rapidly adhere to their surfaces, forming a protective layer that shields them from shear forces, preventing recognition and destruction by immune cells.[18,20] Moreover, platelets are a principal source of TGF-β1, and platelet-tumor cell interaction leads to the abundant release of TGF-β1, which promotes the proliferation of Tregs and simultaneously inhibits the activity of NK cells, DCs, and effector T cells.[40–43] The immunosuppression mediated by TGF-β1 significantly contributes to the ineffectiveness

(D and E) Flow cytometry analysis of NKG2D and CD107a expression on NK cells (D) and CD80 and CD86 expression on DCs (E) in peripheral blood after various treatments.

(F and G) Flow cytometry analysis of IFN-γ and granzyme B secretion by $CD3^+CD8^+$ T cells in the peripheral blood (F) and spleen (G) at the end of treatment. Data are presented as mean ± SD, $n = 5$ mice for each group. Statistical significance was analyzed by one-way ANOVA with Dunnett's test. $^*p < 0.05$, $^{**}p < 0.01$, $^{***}p < 0.001$, $^{****}p < 0.0001$.

of PD-1 blockade therapies.[44,45] Of note, beyond their well-established roles in hemostasis and tumor metastasis, recent studies have identified platelets as immune cells with both anti-inflammatory and pro-inflammatory functions,[27,28,46] emphasizing the crucial need to maintain normal platelet function. Given that hyperactive TAPs, a small proportion of circulating platelets, are key facilitators of tumor metastasis and immune evasion, our study focused on the impact of selectively eliminating TAPs on enhancing the anti-metastatic efficacy of aPD-1 treatments, while largely sparing the majority of resting platelets unaffected. Leveraging the abundantly expressed active GPIIb/IIIa receptors on activated/hyperactive platelets, we achieved the precise depletion of hyperactive TAPs in the circulation and metastasis sites by developing TAP-targeted, ABT-737-loaded cRGD-NP@A nanoparticles. Given that tumor cells can activate platelets through multiple receptors and existing antiplatelet drugs only target single pathways, ABT-737, a well-known inducer of platelet apoptosis, was employed to induce the apoptosis of TAPs for the effective prevention of platelet-tumor cell crosstalk.[29,47] Using mouse and rat experimental metastasis models and the patient-derived metastasis model, our results demonstrate that the specific apoptotic elimination of TAPs with cRGD-NP@A boosts the immune response of PD-1 blockade therapy by not only promoting the exposure of tumor cells to the immune system but also alleviating the immunosuppressive effects mediated by TAP-derived TGF-β1. In particular, the combination of cRGD-NP@A with aPD-1 dramatically augmented immune activation with enhanced function of NK cells, DCs, and CTLs in the peripheral blood, with increased secretion of granzyme B and IFN-γ by $CD8^+$ T cells in the spleen. Safety assessment results indicate that multiple treatments with cRGD-NP@A did not lead to hemostatic dysfunction or bleeding in the major organs of healthy mice, demonstrating the precise targeting of TAPs and negligible effects on resting platelets of our nanodrug *in vivo*.

Numerous studies have been dedicated to enhancing the efficacy of immune checkpoint blockade therapy across preclinical and clinical settings. The TME plays a pivotal role in tumor immune surveillance, and given the greater genomic stability of non-tumor versus tumor cells, optimizing the TME to rescue T cell dysfunction is a key area of interest.[48,49] However, the TME is characterized by complex and dynamic cellular interactions that challenge precise targeting and modulation, as cells of the same type can exhibit diverse, sometimes contradictory, effects on tumor immunity.[50,51] Among TME components, platelets represent a relatively accessible target due to their stable presence in circulation and consistent proteomic profiles. Additionally, the significant role of platelets in various stages of tumor metastasis, including immune evasion, aligns with the use of PD-1/PD-L1 blockade therapy primarily in advanced/metastatic cancers. Our cRGD-NP@A nanodrug is designed to potentiate the immune efficacy of aPD-1 antibodies while mitigating platelet support in tumor metastasis, thereby synergistically enhancing the anti-metastatic effects of PD-1 blockade therapy. This strategy offers a safe and effective means to improve both the immune response rate and the anti-metastatic effectiveness of PD-1 blockade therapy in metastatic cancer treatment.

Limitations of the study

While our study provides compelling evidence for the therapeutic potential of cRGD-NP@A in enhancing PD-1 blockade therapy, several limitations should be acknowledged. Firstly, the majority of our experiments relied on the B16-F10 melanoma model; thus, comprehensive validation across a broader range of tumor models is crucial to confirm the applicability and the mechanisms of action of cRGD-NP@A. Furthermore, additional studies are needed to support clinical translation, such as precise optimization of dosage and consideration of tumor-specific characteristics. Finally, despite the relatively simple design of our nanosystem, achieving its scalable and reproducible manufacturing remains a critical challenge for future clinical applications.

RESOURCE AVAILABILITY

Lead contact

Further information and requests for resources and reagents should be directed to and will be fulfilled by the lead contact, Suping Li (lisuping@nanoctr.cn).

Materials availability

This study did not generate new unique reagents.

Data and code availability

- NMR raw data have been deposited at figshare (https://doi.org/10.6084/m9.figshare.28308650) and are publicly available. Accession numbers are listed in the key resources table.
- This study did not report original code.
- Any additional information required to reanalyze the data reported in this paper is available from the lead contact upon request.

ACKNOWLEDGMENTS

This work was financially supported by the National Key R&D Program of China (nos. 2022YFA1207300 and 2023YFC3403100) (S.L.), the National Natural Science Foundation of China (82472141) (S.L.), the CAS Project for Young Scientists in Basic Research (no. YSBR-036) (S.L.), the Beijing Natural Science Foundation Economic-Technological Development Area Innovation Joint Fund (no. L248091) (S.L.), and the Strategic Priority Research Program of Chinese Academy of Sciences (XDB36000000) (G.N.).

AUTHOR CONTRIBUTIONS

S.L., G.N., Y.Z., and S.W. conceptualized and designed the research. S.W. conducted the experiments, analyzed the data, and drafted the manuscript. Z.W. assisted with animal experiments. Z.L., F.Q., J.C., T.C., and B.L. contributed to data analysis and sample collection. S.L. critically revised the manuscript and provided overall supervision and guidance for the project.

DECLARATION OF INTERESTS

The authors declare no competing interests.

STAR★METHODS

Detailed methods are provided in the online version of this paper and include the following:

- KEY RESOURCES TABLE
- EXPERIMENTAL MODEL AND STUDY PARTICIPANT DETAILS
  - Cell lines
  - Animal models
- METHOD DETAILS
  - Isolation of mouse platelets

- Tumor cell-platelet co-culture
- Flow cytometry analysis of circulating platelet activation
- Targeting abilities of free cRGD/PSN peptide for activated platelets and TAPs
- Synthesis of cRGD-NP@A nanoparticles
- Characterization of cRGD-NP@A nanoparticles
- Drug loading and release
- *In vitro* cellular uptake behavior of cRGD-modified nanoparticles
- *In vitro* platelet apoptosis induction by cRGD-NP@A
- Evaluation of targeting ability of cRGD-NP@A *in vivo*
- Investigation of platelet-tumor cell adhesion *in vivo*
- Impact of cRGD-NP@A on tumor cell-induced platelet activation and coagulation function
- *In vivo* anti-metastasis assay
- Co-culture of PBMCs and cancer cells *in vitro*
- Flow cytometry analysis of immune response *in vivo*
- Flow cytometry analysis of apoptosis in major circulatory immune cells
- Flow cytometry analysis of megakaryocytes
- Biosafety evaluation
- Hemolysis assay

- QUANTIFICATION AND STATISTICAL ANALYSIS

SUPPLEMENTAL INFORMATION

Supplemental information can be found online at https://doi.org/10.1016/j.xcrm.2025.101984.

Received: May 9, 2024
Revised: October 24, 2024
Accepted: January 31, 2025
Published: February 27, 2025

REFERENCES

1. Hanahan, D., and Weinberg, R.A. (2011). Hallmarks of Cancer: The Next Generation. Cell *144*, 646–674. https://doi.org/10.1016/j.cell.2011.02.013.
2. Dong, H., Strome, S.E., Salomao, D.R., Tamura, H., Hirano, F., Flies, D.B., Roche, P.C., Lu, J., Zhu, G., Tamada, K., et al. (2002). Tumor-associated B7-H1 promotes T-cell apoptosis: A potential mechanism of immune evasion. Nat. Med. *8*, 793–800. https://doi.org/10.1038/nm730.
3. Freeman, G.J., Long, A.J., Iwai, Y., Bourque, K., Chernova, T., Nishimura, H., Fitz, L.J., Malenkovich, N., Okazaki, T., Byrne, M.C., et al. (2000). Engagement of the PD-1 immunoinhibitory receptor by a novel B7 family member leads to negative regulation of lymphocyte activation. J. Exp. Med. *192*, 1027–1034. https://doi.org/10.1084/jem.192.7.1027.
4. Iwai, Y., Ishida, M., Tanaka, Y., Okazaki, T., Honjo, T., and Minato, N. (2002). Involvement of PD-L1 on tumor cells in the escape from host immune system and tumor immunotherapy by PD-L1 blockade. Proc. Natl. Acad. Sci. USA *99*, 12293–12297. https://doi.org/10.1073/pnas.192461099.
5. Morad, G., Helmink, B.A., Sharma, P., and Wargo, J.A. (2021). Hallmarks of response, resistance, and toxicity to immune checkpoint blockade. Cell *184*, 5309–5337. https://doi.org/10.1016/j.cell.2021.09.020.
6. Nguyen, D.X., Bos, P.D., and Massagué, J. (2009). Metastasis: from dissemination to organ-specific colonization. Nat. Rev. Cancer *9*, 274–284. https://doi.org/10.1038/nrc2622.
7. Gay, L.J., and Felding-Habermann, B. (2011). Contribution of platelets to tumour metastasis. Nat. Rev. Cancer *11*, 123–134. https://doi.org/10.1038/nrc3004.
8. Haemmerle, M., Stone, R.L., Menter, D.G., Afshar-Kharghan, V., and Sood, A.K. (2018). The Platelet Lifeline to Cancer: Challenges and Opportunities. Cancer Cell *33*, 965–983. https://doi.org/10.1016/j.ccell.2018.03.002.
9. Li, S., Lu, Z., Wu, S., Chu, T., Li, B., Qi, F., Zhao, Y., and Nie, G. (2024). The dynamic role of platelets in cancer progression and their therapeutic implications. Nat. Rev. Cancer *24*, 72–87. https://doi.org/10.1038/s41568-023-00639-6.
10. Miao, S., Shu, D., Zhu, Y., Lu, M., Zhang, Q., Pei, Y., He, A.D., Ma, R., Zhang, B., and Ming, Z.Y. (2019). Cancer cell-derived immunoglobulin G activates platelets by binding to platelet FcγRIIa. Cell Death Dis. *10*, 87. https://doi.org/10.1038/s41419-019-1367-x.
11. Xu, X.R., Yousef, G.M., and Ni, H. (2018). Cancer and platelet crosstalk: opportunities and challenges for aspirin and other antiplatelet agents. Blood *131*, 1777–1789. https://doi.org/10.1182/blood-2017-05-743187.
12. t Veld, S.G.J.G., and Wurdinger, T. (2019). Tumor-educated platelets. Blood *133*, 2359–2364. https://doi.org/10.1182/blood-2018-12-852830.
13. Dymicka-Piekarska, V., Koper-Lenkiewicz, O.M., Zińczuk, J., Kratz, E., and Kamińska, J. (2020). Inflammatory cell-associated tumors. Not only macrophages (TAMs), fibroblasts (TAFs) and neutrophils (TANs) can infiltrate the tumor microenvironment. The unique role of tumor associated platelets (TAPs). Cancer Immunol. Immunother. *70*, 1497–1510. https://doi.org/10.1007/s00262-020-02758-7.
14. Labelle, M., Begum, S., and Hynes, R.O. (2014). Platelets guide the formation of early metastatic niches. Proc. Natl. Acad. Sci. USA *111*, E3053–E3061. https://doi.org/10.1073/pnas.1411082111.
15. Menter, D.G., Hatfield, J.S., Harkins, C., Sloane, B.F., Taylor, J.D., Crissman, J.D., and Honn, K.V. (1987). Tumor cell-platelet interactions in vitro and their relationship to in vivo arrest of hematogenously circulating tumor cells. Clin. Exp. Metastasis *5*, 65–78. https://doi.org/10.1007/BF00116627.
16. Kim, Y.J., Borsig, L., Varki, N.M., and Varki, A. (1998). P-selectin deficiency attenuates tumor growth and metastasis. Proc. Natl. Acad. Sci. USA *95*, 9325–9330. https://doi.org/10.1073/pnas.95.16.9325.
17. McCarty, O.J.T., Mousa, S.A., Bray, P.F., and Konstantopoulos, K. (2000). Immobilized platelets support human colon carcinoma cell tethering, rolling, and firm adhesion under dynamic flow conditions. Blood *96*, 1789–1797. https://doi.org/10.1182/blood.V96.5.1789.
18. Nieswandt, B., Hafner, M., Echtenacher B Fau - Männel, D.N., and Männel, D.N. (1999). Lysis of tumor cells by natural killer cells in mice is impeded by platelets. Cancer Res. *59*, 1295–1300.
19. Philippe, C., Philippe, B., Fouqueray, B., Perez, J., Lebret, M., and Baud, L. (1993). Protection from tumor necrosis factor-mediated cytolysis by platelets. Am. J. Pathol. *143*, 1713–1723.
20. Placke, T., Örgel, M., Schaller, M., Jung, G., Rammensee, H.-G., Kopp, H.-G., and Salih, H.R. (2012). Platelet-Derived MHC Class I Confers a Pseudonormal Phenotype to Cancer Cells That Subverts the Antitumor Reactivity of Natural Killer Immune Cells. Cancer Res. *72*, 440–448. https://doi.org/10.1158/0008-5472.Can-11-1872.
21. Labelle, M., Begum, S., and Hynes, R.O. (2011). Direct Signaling between Platelets and Cancer Cells Induces an Epithelial-Mesenchymal-Like Transition and Promotes Metastasis. Cancer Cell *20*, 576–590. https://doi.org/10.1016/j.ccr.2011.09.009.
22. Schumacher, D., Strilic, B., Sivaraj, K.K., Wettschureck, N., and Offermanns, S. (2013). Platelet-Derived Nucleotides Promote Tumor-Cell Transendothelial Migration and Metastasis via P2Y2 Receptor. Cancer Cell *24*, 130–137. https://doi.org/10.1016/j.ccr.2013.05.008.
23. Chai, S., Matsumoto, N., Storgard, R., Peng, C.C., Aparicio, A., Ormseth, B., Rappard, K., Cunningham, K., Kolatkar, A., Nevarez, R., et al. (2021). Platelet-Coated Circulating Tumor Cells Are a Predictive Biomarker in Patients with Metastatic Castrate-Resistant Prostate Cancer. Mol. Cancer Res. *19*, 2036–2045. https://doi.org/10.1158/1541-7786.MCR-21-0383.
24. Yamaguchi, T., Fushida, S., Kinoshita, J., Okazaki, M., Ishikawa, S., Ohbatake, Y., Terai, S., Okamoto, K., Nakanuma, S., Makino, I., et al. (2020). Extravasated platelet aggregation contributes to tumor progression via the accumulation of myeloid-derived suppressor cells in gastric cancer with

peritoneal metastasis. Oncol. Lett. *20*, 1879–1887. https://doi.org/10.3892/ol.2020.11722.

25. Huang, J., Jochems, C., Talaie, T., Anderson, A., Jales, A., Tsang, K.Y., Madan, R.A., Gulley, J.L., and Schlom, J. (2012). Elevated serum soluble CD40 ligand in cancer patients may play an immunosuppressive role. Blood *120*, 3030–3038. https://doi.org/10.1182/blood-2012-05-427799.
26. Ay, C., Simanek, R., Vormittag, R., Dunkler, D., Alguel, G., Koder, S., Kornek, G., Marosi, C., Wagner, O., Zielinski, C., and Pabinger, I. (2008). High plasma levels of soluble P-selectin are predictive of venous thromboembolism in cancer patients: results from the Vienna Cancer and Thrombosis Study (CATS). Blood *112*, 2703–2708. https://doi.org/10.1182/blood-2008-02-142422.
27. Li, J., Karakas, D., Xue, F., Chen, Y., Zhu, G., Yucel, Y.H., MacParland, S.A., Zhang, H., Semple, J.W., Freedman, J., et al. (2023). Desialylated Platelet Clearance in the Liver is a Novel Mechanism of Systemic Immunosuppression. Research *6*, 0236. https://doi.org/10.34133/research.0236.
28. Xu, X.R., Zhang, D., Oswald, B.E., Carrim, N., Wang, X., Hou, Y., Zhang, Q., Lavalle, C., McKeown, T., Marshall, A.H., and Ni, H. (2016). Platelets are versatile cells: New discoveries in hemostasis, thrombosis, immune responses, tumor metastasis and beyond. Crit. Rev. Clin. Lab Sci. *53*, 409–430. https://doi.org/10.1080/10408363.2016.1200008.
29. Vogler, M., Hamali, H.A., Sun, X.-M., Bampton, E.T.W., Dinsdale, D., Snowden, R.T., Dyer, M.J.S., Goodall, A.H., and Cohen, G.M. (2011). BCL2/BCL-XL inhibition induces apoptosis, disrupts cellular calcium homeostasis, and prevents platelet activation. Blood *117*, 7145–7154. https://doi.org/10.1182/blood-2011-03-344812.
30. Boone, B.A., Murthy, P., Miller-Ocuin, J., Doerfler, W.R., Ellis, J.T., Liang, X., Ross, M.A., Wallace, C.T., Sperry, J.L., Lotze, M.T., et al. (2018). Chloroquine reduces hypercoagulability in pancreatic cancer through inhibition of neutrophil extracellular traps. BMC Cancer *18*, 678. https://doi.org/10.1186/s12885-018-4584-2.
31. Yu, L.X., Yan, L., Yang, W., Wu, F.Q., Ling, Y., Chen, S.Z., Tang, L., Tan, Y.X., Cao, D., Wu, M.C., et al. (2014). Platelets promote tumour metastasis via interaction between TLR4 and tumour cell-released high-mobility group box1 protein. Nat. Commun. *5*, 5256. https://doi.org/10.1038/ncomms6256.
32. Cheng, S., Craig, W.S., Mullen, D., Tschopp, J.F., Dixon, D., and Pierschbacher, M.D. (1994). Design and synthesis of novel cyclic RGD-containing peptides as highly potent and selective integrin .alpha.IIb.beta.3 antagonists. J. Med. Chem. *37*, 1–8. https://doi.org/10.1021/jm00027a001.
33. Molenaar, T.J.M., Appeldoorn, C.C.M., de Haas, S.A.M., Michon, I.N., Bonnefoy, A., Hoylaerts, M.F., Pannekoek, H., van Berkel, T.J.C., Kuiper, J., and Biessen, E.A.L. (2002). Specific inhibition of P-selectin-mediated cell adhesion by phage display-derived peptide antagonists. Blood *100*, 3570–3577. https://doi.org/10.1182/blood-2002-02-0641.
34. Zucchella, M., Dezza, L., Pacchiarini, L., Meloni, F., Tacconi, F., Bonomi, E., Grignani, G., and Notario, A. (1989). Human tumor cells cultured "in vitro" activate platelet function by producing ADP or thrombin. Haematologica *74*, 541–545.
35. Haemmerle, M., Bottsford-Miller, J., Pradeep, S., Taylor, M.L., Choi, H.J., Hansen, J.M., Dalton, H.J., Stone, R.L., Cho, M.S., Nick, A.M., et al. (2016). FAK regulates platelet extravasation and tumor growth after antiangiogenic therapy withdrawal. J. Clin. Investig. *126*, 1885–1896. https://doi.org/10.1172/JCI85086.
36. Zhao, J., Qi, Q., Yang, Y., Gu, H.Y., Lu, N., Liu, W., Wang, W., Qiang, L., Zhang, L.B., You, Q.D., and Guo, Q.L. (2008). Inhibition of α4 integrin mediated adhesion was involved in the reduction of B16-F10 melanoma cells lung colonization in C57BL/6 mice treated with gambogic acid. Eur. J. Pharmacol. *589*, 127–131. https://doi.org/10.1016/j.ejphar.2008.04.063.
37. Bai, J., Zhang, J., Wu, J., Shen, L., Zeng, J., Ding, J., Wu, Y., Gong, Z., Li, A., Xu, S., et al. (2010). JWA regulates melanoma metastasis by integrin alphaVbeta3 signaling. Oncogene *29*, 1227–1237. https://doi.org/10.1038/onc.2009.408.
38. Lucas, K.M., Mohana-Kumaran, N., Lau, D., Zhang, X.D., Hersey, P., Huang, D.C., Weninger, W., Haass, N.K., and Allen, J.D. (2012). Modulation of NOXA and MCL-1 as a strategy for sensitizing melanoma cells to the BH3-mimetic ABT-737. Clin. Cancer Res. *18*, 783–795. https://doi.org/10.1158/1078-0432.CCR-11-1166.
39. Roweth, H.G., and Battinelli, E.M. (2021). Lessons to learn from tumor-educated platelets. Blood *137*, 3174–3180. https://doi.org/10.1182/blood.2019003976.
40. Tauriello, D.V.F., Sancho, E., and Batlle, E. (2022). Overcoming TGFβ-mediated immune evasion in cancer. Nat. Rev. Cancer *22*, 25–44. https://doi.org/10.1038/s41568-021-00413-6.
41. Thomas, D.A., and Massagué, J. (2005). TGF-β directly targets cytotoxic T cell functions during tumor evasion of immune surveillance. Cancer Cell *8*, 369–380. https://doi.org/10.1016/j.ccr.2005.10.012.
42. Weber, F., Byrne, S.N., Le, S., Brown, D.A., Breit, S.N., Scolyer, R.A., and Halliday, G.M. (2005). Transforming growth factor-β1 immobilises dendritic cells within skin tumours and facilitates tumour escape from the immune system. Cancer Immunol. Immunother. *54*, 898–906. https://doi.org/10.1007/s00262-004-0652-3.
43. Rachidi, S., Metelli, A., Riesenberg, B., Wu, B.X., Nelson, M.H., Wallace, C., Paulos, C.M., Rubinstein, M.P., Garrett-Mayer, E., Hennig, M., et al. (2017). Platelets subvert T cell immunity against cancer via GARP-TGFβ axis. Sci. Immunol. *2*, eaai7911. https://doi.org/10.1126/sciimmunol.aai7911.
44. Kalbasi, A., and Ribas, A. (2020). Tumour-intrinsic resistance to immune checkpoint blockade. Nat. Rev. Immunol. *20*, 25–39. https://doi.org/10.1038/s41577-019-0218-4.
45. Sun, Q., Hong, Z., Zhang, C., Wang, L., Han, Z., and Ma, D. (2023). Immune checkpoint therapy for solid tumours: clinical dilemmas and future trends. Signal Transduct. Targeted Ther. *8*, 320. https://doi.org/10.1038/s41392-023-01522-4.
46. Li, C., Ture, S.K., Nieves-Lopez, B., Blick-Nitko, S.K., Maurya, P., Livada, A.C., Stahl, T.J., Kim, M., Pietropaoli, A.P., and Morrell, C.N. (2024). Thrombocytopenia Independently Leads to Changes in Monocyte Immune Function. Circ. Res. *134*, 970–986. https://doi.org/10.1161/CIRCRESAHA.123.323662.
47. Xiang, Y.Z., Kang, L.Y., Gao, X.M., Shang, H.C., Zhang, J.H., and Zhang, B.L. (2008). Strategies for antiplatelet targets and agents. Thromb. Res. *123*, 35–49. https://doi.org/10.1016/j.thromres.2008.05.003.
48. Kubli, S.P., Berger, T., Araujo, D.V., Siu, L.L., and Mak, T.W. (2021). Beyond immune checkpoint blockade: emerging immunological strategies. Nat. Rev. Drug Discov. *20*, 899–919. https://doi.org/10.1038/s41573-021-00155-y.
49. Tang, T., Huang, X., Zhang, G., Hong, Z., Bai, X., and Liang, T. (2021). Advantages of targeting the tumor immune microenvironment over blocking immune checkpoint in cancer immunotherapy. Signal Transduct. Targeted Ther. *6*, 72. https://doi.org/10.1038/s41392-020-00449-4.
50. Binnewies, M., Roberts, E.W., Kersten, K., Chan, V., Fearon, D.F., Merad, M., Coussens, L.M., Gabrilovich, D.I., Ostrand-Rosenberg, S., Hedrick, C.C., et al. (2018). Understanding the tumor immune microenvironment (TIME) for effective therapy. Nat. Med. *24*, 541–550. https://doi.org/10.1038/s41591-018-0014-x.
51. Joyce, J.A. (2005). Therapeutic targeting of the tumor microenvironment. Cancer Cell *7*, 513–520. https://doi.org/10.1158/2159-8290.CD-20-1808.
52. Wulf-Goldenberg, A., Hoffmann, J., Becker, M., Brzezicha, B., and Walther, W. (2021). Patient-Derived Xenografts from Solid Tumors (PDX) for Models of Metastasis. In Metastasis. Methods in Molecular Biology, U.S. Stein, ed. (Humana), pp. 43–58.

STAR★METHODS

KEY RESOURCES TABLE

REAGENT or RESOURCE	SOURCE	IDENTIFIER
Antibodies		
PE anti-mouse CD41 (clone: MWReg30)	BD Biosciences	Cat#558040; RRID: AB_397004
FITC anti-mouse CD41 (clone: MWReg30)	Biolegend	Cat#133904; RRID: AB_1626237
PE anti-mouse integrin αIIbβ3 (clone: JON/A)	Emfret	Cat#M023-2
APC anti-human/mouse CD62P (clone: Psek.KO2.3)	eBioscience	Cat#17-0626-80; RRID: AB_11218294
PE/Cyanine7 anti-mouse CD3 (clone: 17A2)	Biolegend	Cat#100220; RRID: AB_1732057
FITC anti-mouse CD3 (clone: 17A2)	Biolegend	Cat#100204; RRID: AB_312661
FITC anti-mouse CD8a (clone: 53–6.7)	Biolegend	Cat#100706; RRID: AB_312744
PE anti-mouse IFN-γ (clone: XMG1.2)	Biolegend	Cat#505807; RRID: AB_315401
Brilliant Violet 605 anti-mouse IFN-γ (clone: XMG1.2)	Biolegend	Cat#505840; RRID: AB_2561438
APC anti-mouse Ki-67 (clone: 16A8)	Biolegend	Cat#652405; RRID: AB_2561929
PE anti-human/mouse Granzyme B (clone: QA16A02)	Biolegend	Cat#372208; RRID: AB_2687031
PerCP/Cyanine5.5 anti-mouse CD11c (clone: N418)	Biolegend	Cat#117327; RRID: AB_2129641
FITC anti-mouse CD80 (clone: 16-10A1)	Biolegend	Cat#104705; RRID: AB_313126
PE anti-mouse CD86 (clone: GL-1)	Biolegend	Cat#105007; RRID: AB_313150
Brilliant Violet 421 anti-mouse NK-1.1 (clone: PK136)	Biolegend	Cat#108731; RRID: AB_10895916
PE anti-mouse NKG2D (clone: CX5)	Biolegend	Cat#130207; RRID: AB_1227712
APC anti-mouse CD107a (clone: 1D4B)	Biolegend	Cat#121613; RRID: AB_2234505
Alexa Fluor 647 anti-mouse CD4 (clone: RM4-5)	Biolegend	Cat#100533; RRID: AB_493372
PE anti-mouse FOXP3 (clone: MF-14)	Biolegend	Cat#126403; RRID: AB_1089117
PE anti-mouse Ly-6C (clone: HK1.4)	Biolegend	Cat#128007; RRID: AB_1186132
FITC anti-mouse Ly-6G (clone: 1A8)	Biolegend	Cat#127605; RRID: AB_1236488
PE/Cyanine5 anti-mouse CD19 (clone: 6D5)	Biolegend	Cat#115509; RRID: AB_313645
PE/Cyanine5 anti-mouse/human CD11b (clone: M1/70)	Elabscience	Cat#E-AB-F1081G
CD41 polyclonal antibody	Invitrogen	Cat#PA5-79527; RRID: AB_2746643
P-Selectin monoclonal antibody (clone: H-2)	Santa Cruz Biotechnology	Cat#sc-271267
FOXP3 monoclonal antibody (clone: D6O8R)	Cell Signaling	Cat#12653T
CD8α monoclonal antibody (clone: D4W2Z)	Cell Signaling	Cat#98941T
*InVivo*MAb anti-mouse PD-1 (clone: RMP1-14)	Bio X Cell	Cat#BE0146; RRID: AB_10949053
Biological samples		
Human blood	The Second Hospital of Tianjin Medical University	ID: KY2024K305
Patient-derived tumor tissue	The Second Hospital of Tianjin Medical University	ID: KY2024K305
Chemicals, peptides, and recombinant proteins		
Prostaglandin E1	MCE	Cat#HY-B0131
SB-431542	MCE	Cat#HY-10431
ABT-737	Selleck	Cat#S1002
Cy5.5	Meryer	Cat#M81813
Cy5	Meryer	Cat#M81811
Citric acid	Sigma-Aldrich	Cat#27109
Sodium citrate	Sigma-Aldrich	Cat#C3674
Dextrose	Sigma-Aldrich	Cat#D9434
Sodium cholate	Macklin	Cat#S821473

(*Continued on next page*)

Continued

REAGENT or RESOURCE	SOURCE	IDENTIFIER
Human TGF-beta 1 recombinant protein	PeproTech	Cat#100-21-10UG
cRGD peptide (CNPRGDY(OEt)RC)	Guoping Pharmaceutical Co., Ltd.	N/A
Poly(lactic-co-glycolic acid)-methoxy-poly(ethylene glycol) (75:25, $PLGA_{15k}$-$mPEG_{5k}$)	Jinan Daigang Biomaterial Co., Ltd.	N/A
Poly(lactic-co-glycolic acid)-b-poly (ethylene glycol)-N-hydroxysuccinimide (75:25, $PLGA_{15k}$-PEG_{5k}-NHS)	Xi'an ruixi Biological Technology Co., Ltd.	N/A
Critical commercial assays		
Mouse TNF-α ELISA Kit	Solarbio	Cat#SEKM-0034
Mouse IL-6 ELISA Kit	Solarbio	Cat#SEKM-0007
Mouse IL-2 ELISA Kit	Solarbio	Cat#SEKM-0004
Mouse IFN-γ ELISA Kit	Solarbio	Cat#SEKM-0031
Mouse TGF-β1 ELISA Kit	Solarbio	Cat#SEKM-0035
Mouse SELP (P-Selectin) ELISA Kit	Elabscience	Cat#E-EL-M0638
Mouse TSP-1 (Thrombospondin-1) ELISA Kit	Elabscience	Cat#E-EL-M3083
Deposited data		
NMR raw data files	This paper	figshare: https://doi.org/10.6084/m9.figshare.28308650
Experimental models: Cell lines		
Murine B16-F10 melanoma cell line	ATCC	Cat#CRL-6475
Murine LLC Lewis lung carcinoma cell line	ATCC	Cat#CRL-1642
Rat MADB106 breast cancer cell line	KCB	Cat#KCB2013045YJ
Experimental models: Organisms/strains		
Mouse: C57BL/6N	Vital River	N/A
Mouse: BALB/c nude	Vital River	N/A
Rat: F344	Vital River	N/A
Software and algorithms		
GraphPad Prism (version 10.1.2)	GraphPad Software	https://www.graphpad.com/
FlowJo (version 10.8.1)	BD Biosciences	https://www.flowjo.com/
Living Image (version 4.1)	Caliper Life Sciences	https://living-image.software.informer.com/4.1/
Adobe Illustrator	Adobe	https://www.adobe.com/products/illustrator/free-trial-download.html
Other		
Intracellular Staining Perm Wash Buffer	Biolegend	Cat#421002
Human CD3/CD28/CD2 T cell Activator	STEMCELL	Cat#10970
Modified Tyrode's solution	Solarbio	Cat#T1420
Dulbecco's modified Eagle medium	Wisent	Cat#319-005-CL
RPMI 1640 medium	Wisent	Cat#350-000-CL
Fetal bovine serum	Wisent	Cat#085–150
Penicillin-Streptomycin solution	Wisent	Cat#450-201-EL
CellMask Orange Plasma Membrane Stain	Invitrogen	Cat#C10045

EXPERIMENTAL MODEL AND STUDY PARTICIPANT DETAILS

Cell lines

Murine B16-F10 melanoma cells (ATCC, CRL-6475), LLC Lewis lung carcinoma cells (ATCC, CRL-1642), and MADB106 breast cancer cells (KCB, KCB2013045YJ) were purchased from Procell Life Science & Technology Co., Ltd. (Wuhan, China). The cells were cultured in Dulbecco's modified Eagle medium (DMEM) containing 10% fetal bovine serum (FBS, Cat#085–150), 100 units/mL of penicillin, and 100 μg/mL of streptomycin (Cat#450-201-EL). All cells were incubated in a 5% CO_2 atmosphere at 37°C.

Animal models

Female C57BL/6N mice, female BALB/c nude mice, and male F344 rats of 6–8 weeks were purchased from Beijing Vital River Laboratory Animal Technology Co., Ltd. Animals were maintained under pathogen-free conditions with optimal temperature and humidity. All animal experiments were approved by the Institutional Animal Care and Use Committee (IACUC) of the National Center for Nanoscience and Technology.

To establish a subcutaneous melanoma model, C57BL/6N mice were subcutaneously inoculated with 2×10^5 B16-F10 cells. For murine metastasis models, C57BL/6N mice were intravenously injected with 2×10^5 B16-F10 cells or 1.2×10^6 LLC cells, while F344 rats received 1×10^5 MADB106 cells via intravenous injection. For patient-derived metastasis model, tumor cell suspensions derived from bladder cancer patients were intravenously injected into BALB/c nude mice according to a previously described method with little modifications.[52] The study protocol was approved by the by the Ethics Committee of The Second Hospital of Tianjin Medical University (approval ID, KY2024K305). Surgically removed bladder cancer specimens were obtained from the Department of Urology at the Tianjin Institute of Urology, the Second Hospital of Tianjin Medical University, with written informed consent signed prior to obtaining the samples. The tumor tissue specimen was first subcutaneously implanted into BALB/c nude mice and passed for metastasis model construction. Before use, the tumor tissue was collected, cut into small pieces and subjected to enzymatic digestion (collagenase IV, 300 U/mL) for 1 h at 37°C till the solution turned cloudy. DMEM supplemented with 10% FBS was used to stop enzymatic digestion. The cell suspension was filtrated through a 70 μm cell strainer and washed three times with DMEM to remove FBS. The cells were then resuspended in phosphate-buffered saline (PBS) and the concentration was adjusted to 5×10^6/mL. Then, 0.2 mL of cell suspension was slowly injected into the tail vein of female BALB/c nude mice.

METHOD DETAILS

Isolation of mouse platelets

Platelets were isolated from freshly drawn mouse blood through two-step centrifugation. Whole blood was first centrifuged at 100 g for 20 min. The obtained platelet-rich plasma was further centrifuged at 1800 g for 5 min to remove platelet-poor plasma. The platelets were washed twice with PBS (containing 2 μM prostaglandin E1 (PGE1)) and resuspended in modified Tyrode's buffer (containing 2 μM PGE1) for further use.

Tumor cell-platelet co-culture

For evaluation of B16-F10 cell-induced platelet activation *in vitro*, washed mouse platelets were prelabeled with CellMask Orange (Cat#C10045) and incubated with B16-F10 cells at 37°C for 1–4 h in serum-free DMEM. Cells were washed at least three times with PBS to remove unbound platelets, fixed with 4% paraformaldehyde for 10 min at room temperature (RT), and stained with anti-CD62P antibody (Cat#sc-271267). For nuclear staining, DAPI was used.

Flow cytometry analysis of circulating platelet activation

Two weeks post-inoculation, blood from tumor-bearing mice was collected into centrifuge tubes containing acid-citrate-dextrose (ACD) buffer (85 mM sodium citrate, 66.6 mM citric acid, 111 mM dextrose, 2 μM PGE1) at a volume ratio of ACD: blood of 1:5. Next, 5 μL of whole blood, 1 μL of PE-*anti*-CD41 (Cat#558040), and 2 μL of APC-*anti*-CD62P (Cat#17-0626-80) were added to 42 μL of PBS. After being incubated for 20 min at RT, the mixture was fixed with 200 μL of 4% paraformaldehyde for 15 min at RT. For platelet activity assessment, 10 μM of ADP was further added to the staining system and processed as above. The stained samples were analyzed with a Beckman flow cytometer (CytoFLEX).

Targeting abilities of free cRGD/PSN peptide for activated platelets and TAPs

The ability of free cRGD peptide (CNPRGDY(OEt)RC) and PSN peptide (DAEWVDVS) to bind activated platelets was investigated by flow cytometry. Washed mouse platelets were stimulated with 20 μM ADP at 37°C for 10 min to prepare activated platelets. Then activated and resting platelets were incubated with fluorescein isothiocyanate (FITC)-modified cRGD peptide (cRGD-FITC) and PSN peptide (PSN-FITC) for 15 min at RT, respectively. The unbound peptide was removed by centrifugation. Platelets were washed once with PBS (containing 2 μM PGE1) and resuspended for analysis. The level of platelet activation was assessed via CD62P staining. For analysis of the binding specificity, resting or activated platelets were incubated with cRGE-FITC or cRGD-FITC for 15 min at RT, respectively. For tumor cell binding assay, B16-F10 cells were incubated with cRGD-FITC for 15 min at RT and washed once with PBS for subsequent flow cytometry analysis.

The targeting ability of free cRGD and PSN peptides toward tumor-associated platelets (TAPs) was investigated via confocal microscopy. B16-F10 tumor cells were incubated with CellMask Orange-labeled platelets for 4 h at 37°C. After washing three times with PBS to remove unbound platelets, cells were incubated with cRGD-FITC or PSN-FITC for 15 min at RT and fixed with 4% paraformaldehyde for 10 min at RT. DAPI staining was used for nuclei localization.

Synthesis of cRGD-NP@A nanoparticles

The cRGD peptide was first covalently conjugated to poly(lactic-co-glycolic acid) (PLGA) via a poly(ethylene glycol) (PEG) linker. Briefly, N-hydroxysuccinimide-functionalized PLGA-PEG (PLGA-PEG-NHS) and cRGD peptide were dissolved in dimethylformamide

at a molar ratio of 1:1.1 and stirred for 12 h at RT. The reaction mixture was then transferred to a dialysis bag (2 kD) and dialyzed against deionized water for 24 h. PLGA-PEG-cRGD was obtained by freeze-drying and the structure was characterized by ^{1}H NMR.

The ABT-737-loaded cRGD-NP@A was prepared by a double emulsion-solvent evaporation method. Briefly, 6 mg of PLGA-mPEG, 4 mg of PLGA-PEG-cRGD, and 1 mg of ABT-737 were dissolved in 1 mL of dichloromethane. For Cy5 or Cy5.5 labeling, Cy5 or Cy5.5 dissolved in dimethyl sulfoxide was added to the PLGA and ABT-737 mixture. After the addition of 200 μL of deionized water, the mixture was ultrasonicated (286 W, 3 min) on ice to form the primary emulsion. Then, 2 mL of 2% sodium cholate aqueous solution was added and ultrasonication (330 W, 5 min) was performed to obtain the secondary emulsion. The resulting emulsion was added to 10 mL of 0.5% sodium cholate aqueous solution drop by drop under stirring and dispersed for 15 min at RT. The residual organic solvent was removed by rotary evaporation under reduced pressure. The nanoparticles were collected by centrifugation at 12000 *g* for 15 min at RT and washed once with deionized water. The retrieved nanoparticles were resuspended in deionized water and stored at 4°C for use.

Characterization of cRGD-NP@A nanoparticles

The nanoparticles were resuspended in deionized water at 0.5 mg/mL and the hydrodynamic size and surface charge were measured by dynamic light scattering (DLS) with Zetasizer Nano ZS90 (Malvern Instruments). For evaluation of the stability at 4°C, cRGD-NP@A was suspended in PBS at the concentration of 10 mg/mL and DLS measurement was performed every day to evaluate its size distribution and changes. For evaluation of the stability at 37°C, cRGD-NP@A was suspended in PBS containing 10% FBS under 100 rpm shaking and hydrodynamic size was measured at indicated time points through DLS. The morphology and physical size of the prepared nanoparticles were observed under a transmission electron microscope (TEM, JEOL 1200-EX) after negative staining with 2% uranyl acetate aqueous solution for 2 min at RT.

Drug loading and release

The ABT-737 encapsulated in the nanoparticles was extracted by acetonitrile and measured by HPLC-UV analysis at a wavelength of 300 nm. The drug encapsulation efficiency was calculated as the ratio of the amount of drug encapsulated in the nanoparticles to the initial amount of drug added. The drug loading capacity of the nanoparticles was determined by the ratio of the amount of drug encapsulated to the mass of the nanoparticles. For drug releasing assay, 20 mg of cRGD-NP@A was resuspended in PBS with pH 5.0 and 7.4, respectively, and then transferred into dialysis bags (10 kD). The bags were placed in 30 mL of PBS and incubated on a shaker (37°C, 100 rpm). At appropriate time points, 0.5 mL of the buffer solution was taken out, and the same volume of fresh PBS was added. Cumulative drug release at various time points was calculated based on the concentrations of ABT-737 in the releasing media.

In vitro cellular uptake behavior of cRGD-modified nanoparticles

To investigate the activated platelet targeting ability of the cRGD-NP@A nanoparticles, unmodified PEG-NP@A nanoparticles were used as control. Platelet suspension was prepared as described above and moderately activated by 20 μM ADP for 10 min at 37°C. Resting and activated platelets were incubated with Cy5.5-labeled PEG-NP@A and cRGD-NP@A, respectively for 30 min at 37°C under gentle shaking. After incubation, the platelets were washed once with PBS (containing 2 μM PGE1) for subsequent flow cytometry analysis.

To explore the uptake behavior of the cRGD-modified nanoparticles by TAPs, AF488-conjugated wheat germ agglutinin (WGA)-labeled platelets were incubated with adherent B16-F10 cells for 20 min at 37°C followed by centrifugation of the co-culture supernatant at 1800 g for 5 min to obtain TAPs *in vitro*. B16-F10-stimulated and control platelets were incubated with Cy5.5-labeled PEG-NP@A and cRGD-NP@A, respectively for 10 min at 37°C, fixed, and subjected to confocal microscopy observation.

To investigate the effects of cRGD modification on the uptake of PLGA nanoparticles by neutrophils, monocytes, B and T lymphocytes, peripheral blood mononuclear cells (PBMCs) isolated from freshly drawn mouse blood were first stained with the following antibody combinations for 20 min at RT: for neutrophil/monocyte analysis, PC5-*anti*-CD11b (Cat#E-AB-F1081G), FITC-*anti*-Ly-6G (Cat#127605), and PE-*anti*-Ly-6C (Cat#128007) were used; for lymphocyte analysis, PC5-*anti*-CD19 (Cat#115509) and FITC-*anti*-CD3 (Cat#100204) were used. Then differently labeled PBMCs were incubated with Cy5-labeled cRGD-NP@A or PEG-NP@A for 30 min at 37°C under gentle shaking, centrifuged at 350 g for 5 min to remove unbound nanoparticles and washed once with PBS for subsequent flow cytometry analysis. Neutrophils were identified as $CD11b^{+}Ly\text{-}6G^{+}Ly\text{-}6C^{+}$ cells, monocytes as $CD11b^{+}Ly\text{-}6G^{-}Ly\text{-}6C^{+}$ cells, B cells as $CD19^{+}$ cells, and T cells as $CD3^{+}$ cells.

In vitro platelet apoptosis induction by cRGD-NP@A

Platelet stimulation by ADP or B16-F10 cells was conducted as described earlier. To verify the efficient induction of apoptosis in activated platelets by cRGD-NP@A, resting and ADP-activated platelets were respectively incubated with cRGD-NP@A with the ABT-737 concentrations of 0.1–5 μM for 2 h at 37°C in RPMI 1640 media under gentle shaking. Further, the apoptosis-inducing effects of cRGD-NP@A in TAPs and resting platelets were investigated, where free ABT-737 (ABT) and unmodified ABT-737-loaded PLGA nanoparticles (PEG-NP@A) were included as controls for different forms of drugs. Resting and B16-F10-stimulated platelets were treated with free ABT-737, PEG-NP@A, and cRGD-NP@A at an equivalent ABT-737 concentrations of 0.5, 1, and 2 μM for 2 h at

37°C. After various treatments, platelet apoptosis was detected through flow cytometric analysis of mitochondrial membrane potential ($\Delta\Psi m$) depolarization by tetramethylrhodamine ethyl ester (TMRE) staining and PS exposure by annexin V-FITC binding.

Evaluation of targeting ability of cRGD-NP@A *in vivo*

Two weeks post tumor inoculation, the B16-F10 metastasis-bearing mice were intravenously injected with Cy5-labeled PEG-NP@A and cRGD-NP@A, and free Cy5 at a Cy5 dose of 0.5 mg/kg. The living fluorescence images of mice were taken at indicated time points with an IVIS spectrum imaging system (PerkinElmer). At 24 h post-injection, mice were sacrificed and major organs were harvested for *ex vivo* imaging. For distribution analysis of cRGD-NP@A within pulmonary metastases, lungs were harvested at 2 h after intravenous injection of Cy5-labeled PEG-NP@A and cRGD-NP@A into B16-F10 lung metastasis-bearing mice. The lungs were frozen sliced and stained for CD41 (Cat#PA5-79527) to assess the colocalization between platelets and cRGD-NP@A.

Investigation of platelet-tumor cell adhesion *in vivo*

Healthy C57BL/6N mice were coinjected with 5×10^5 CellMask Orange-labeled B16-F10 cells and FITC-*anti*-CD41 antibody (Cat#133904) via the contralateral tail veins. One hour later, mice were intravenously administered with saline, cRGD-NP, cRGD-NP@A or intraperitoneally administered with free ABT-737 at an ABT-737 dose of 10 mg/kg, respectively. Lungs were harvested at 4 h post-injection of B16-F10 cells and frozen sliced for confocal microscopy examination.

Impact of cRGD-NP@A on tumor cell-induced platelet activation and coagulation function

C57BL/6N mice bearing B16-F10 lung metastasis were treated with saline, cRGD-NP, ABT-737, and cRGD-NP@A respectively (ABT-737: 10 mg/kg). The treatments began at day 7 post tumor inoculation and three treatments at an interval of 3 days were performed. Healthy C57BL/6N mice were used as the control. For the tail bleeding assay, 12 h after the last treatment, 2 mm of the tail was removed from the tip, and the tail was immediately placed in pre-warmed PBS. The beginning of the bleeding time was recorded as the time of tail tip removal, and the end was considered as cessation of bleeding for 10 s. Then, the blood of mice was collected for determination of platelet CD62P (Cat#17-0626-80) and active GPIIb/IIIa (Cat#M023-2) expression by flow cytometry and key coagulation parameters including activated partial thromboplastin time (APTT), prothrombin time (PT), thrombin time (TT) and fibrinogen (FIB).

In vivo anti-metastasis assay

The B16-F10 or LLC metastasis-bearing mice were randomized into seven groups (n = 5 mice) and treated with saline, cRGD-NP, ABT, cRGD-NP@A, aPD-1, ABT + aPD-1, or cRGD-NP@A + aPD-1, respectively (ABT-737: 10 mg/kg, free ABT-737, *i.p.*; cRGD-NP@A, *i.v.*; aPD-1: 200 μg, *i.p.*). The treatments were performed at 12 h after tumor cell implantation and continued once every three days after that. The body weight of mice was recorded at regular intervals. Lungs were harvested on day 17 and surface metastatic foci were counted. Hematoxylin and eosin (H&E) staining of lung tissue sections was performed to assess metastatic areas. To investigate the infiltration of platelets, Tregs and $CD8^+$ T cells within metastatic nodules, immunofluorescence staining with anti-CD41 (Cat#PA5-79527), anti-FOXP3 (Cat#12653T) and anti-CD8 (Cat#98941T) antibodies was conducted, respectively. For the TGF-β1 investigation experiment, B16-F10 lung metastasis-bearing mice were treated with saline, aPD-1, or cRGD-NP@A + aPD-1, aPD-1 + SB-431542, or cRGD-NP@A + aPD-1 + rTGF-β1, respectively (cRGD-NP@A, 10 mg/kg, *i.v.*; aPD-1: 200 μg, *i.p.*; SB-431542, 10 mg/kg, *i.p.*; rTGF-β1, 0.2 μg, *i.p.*). For nude mice bearing patient-derived metastasis, the cRGD-NP@A (10 mg/kg) treatments were performed at 12 h after tumor cell implantation and continued once every three days for a total of seven treatments. At day 28 post-implantation, the lungs of mice were harvested for antimetastatic efficacy evaluation and pathological examination for GATA3 expression.

For anti-metastasis evaluation in rats, F344 rats bearing MADB106 metastasis were randomly divided into four groups (n = 4 rats) and treated with saline, cRGD-NP, ABT, or cRGD-NP@A at ABT-737 dose of 10 mg/kg every three days for a total of six treatments. The first treatment was performed at 12 h after tumor cell implantation. The body weight of rats was monitored during the whole procedure and the lungs were harvested on day 18 for metastasis evaluation. The blood was collected for safety evaluation including blood routine examination, and determination of biochemistry indicators and coagulation parameters.

Co-culture of PBMCs and cancer cells *in vitro*

Written informed consent was signed before obtaining blood from bladder cancer patients for PBMC and platelet isolation and the experimental process was approved by the Ethics Committee of The Second Hospital of Tianjin Medical University (approval ID, KY2024K305). Human PBMCs stimulated with CD3/CD28/CD2 (Cat#10970) for three days were used for the co-culture experiment. Tumor cells derived from bladder cancer patients were seeded and incubated overnight to allow for attachment. PBMCs were then added at an effector-to-target cell ratio of 10:1, followed by the addition of human platelets (3×10^8/mL), Tislelizumab (100 μg/mL), and cRGD-NP@A (ABT-737: 2 μM) in different groups. After incubation for 10 h, tumor cells were harvested by digestion and stained with annexin V to assess apoptosis.

Flow cytometry analysis of immune response *in vivo*

Systemic immune response was evaluated at the end of the anti-metastasis experiment in the B16-F10 model. To examine the activation of $CD8^+$ T cells activation in the spleen, spleen tissues were cut into small pieces, ground, and passed through a 70-μm cell strainer. Red blood cells (RBCs) were lysed with ACK lysis buffer. Then, the single-cell suspensions were stained using the following anti-mouse antibody combinations: PC7-*anti*-CD3 (Cat#100220), FITC-*anti*-CD8 (Cat#100706), PE-*anti*-IFN-γ (Cat#505807), APC-*anti*-Ki 67 (Cat#652405); or PC7-*anti*-CD3, FITC-*anti*-CD8, PE-*anti*-Granzyme B (Cat#372208). Meanwhile, to evaluate the activation of $CD8^+$ T cells in peripheral blood, blood was collected via cardiac puncture and red blood cells were lysed to isolate lymphocytes. The following antibody combinations were used for staining: PC7-*anti*-CD3, FITC-*anti*-CD8, BV605-*anti*-IFN-γ (Cat#505840), PE-*anti*-Granzyme B. For DC analysis, PerCP/Cy5.5-*anti*-CD11c (Cat#117327), FITC-*anti*-CD80 (Cat#104705), and PE-*anti*-CD86 (Cat#105007) were used. For NK cell analysis, BV421-*anti*-NK1.1 (Cat#108731), PE-*anti*-NKG2D (Cat#130207), and APC-*anti*-CD107a (Cat#121613) were used. For Treg analysis, PC7-*anti*-CD3, AF647-*anti*-CD4 (Cat#100533), and PE-*anti*-FOXP3 (Cat#126403) were used.

Flow cytometry analysis of apoptosis in major circulatory immune cells

PBMCs were isolated from healthy C57BL/6N mice 4 h post intravenous injection of cRGD-NP@A and stained with the following antibody combinations for 20 min at RT: for neutrophil/monocyte analysis, PC5-*anti*-CD11b, FITC-*anti*-Ly-6G, and PE-*anti*-Ly-6C were used; for lymphocyte analysis, PC5-*anti*-CD19 and FITC-*anti*-CD3 were used. The samples were then washed once with PBS, incubated with APC-annexin V for another 15 min at RT to stain PS, and subjected to flow cytometry analysis.

Flow cytometry analysis of megakaryocytes

Bone marrow cells were extracted from the femurs at 6 h post intravenous injection of Cy5-labeled cRGD-NP@A nanoparticles into healthy C57BL/6N mice, filtrated through a 70 μm cell strainer. After red blood cell lysis with ACK lysis buffer, the cells were stained with PE-*anti*-CD41 for 20 min at RT, washed once with PBS, and stained PS with FITC-annexin V for 15 min at RT.

Biosafety evaluation

Healthy female C57BL/6N mice were treated with saline, cRGD-NP, ABT, cRGD-NP@A, aPD-1, ABT + aPD-1, or cRGD-NP@A + aPD-1, respectively (ABT-737: 10 mg/kg, free ABT-737, *i.p.*; cRGD-NP@A, *i.v.*; aPD-1: 200 μg, *i.p.*) every three days for a total of six treatments. One day after the last treatment, mice were sacrificed. Blood and major organs (heart, liver, spleen, lung, kidney) were collected for examination. Main biochemical indicators including alanine transaminase (ALT), aspartate aminotransferase (AST), creatine kinase (CK), lactate dehydrogenase (LDH), creatinine (CREA), and blood urea nitrogen (BUN) were determined to evaluate liver, heart and kidney function. H&E staining was performed to assess histological damage in major organs.

Hemolysis assay

RBCs were isolated from freshly drawn whole blood from healthy C57BL/6N mice by centrifugation at 800*g* for 10 min. The RBCs were washed thoroughly with ice-cold PBS until the supernatant turned clear. Then the RBCs were diluted at 1:50 with PBS, followed by the addition of various treatments. After incubation for 2 h at 37°C, the suspension was centrifuged again and the supernatant absorbance at 541 nm was measured. The Triton X-100 group served as a positive control, of which the hemolytic rate was calculated as 100%.

QUANTIFICATION AND STATISTICAL ANALYSIS

All data were presented as the mean ± standard derivation (SD). Statistical analysis between two groups was determined by Student's t test and one-way or two-way ANOVA test was used for comparison among multiple groups. The survival curves of metastasis-bearing mice were determined via log rank (Mantel-Cox) test. The threshold for statistical significance was set at $p < 0.05$. p values were represented as $^*p < 0.05$, $^{**}p < 0.01$, $^{***}p < 0.001$, $^{****}p < 0.0001$; ns, $p > 0.05$. All data in this study were analyzed with GraphPad Prism 10.1.2 software.